ACS OMEGA

http://pubs.acs.org/journal/acsodf

Article

# Structure–Activity Relationship of Lanthanide-Incorporated Nano-Hydroxyapatite for the Adsorption of Fluoride and Lead

A. K. D. Veromee Kalpana Wimalasiri, M. Shanika Fernando, Karolina Dziemidowicz, Gareth R. Williams, K. Rasika Koswattage, D. P. Dissanayake, K. M. Nalin de Silva, and Rohini M. de Silva*

Cite This: *ACS Omega* 2021, 6, 13527–13543

Read Online

ACCESS | Metrics & More | Article Recommendations | Supporting Information

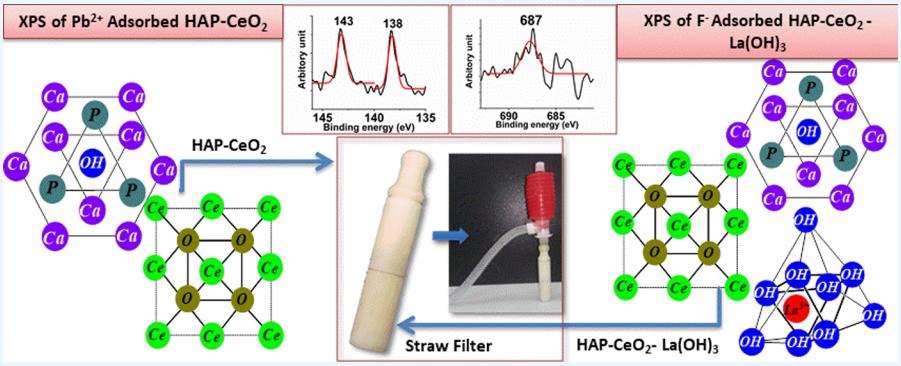


**ABSTRACT:** The growing demand for water purification provided the initial momentum to produce lanthanide-incorporated nano-hydroxyapatite (HAP) such as HAP·$CeO_2$, HAP·$CeO_2$·$La(OH)_3$ (2:1), and HAP·$CeO_2$·$La(OH)_3$ (3:2). These materials open avenues to remove fluoride and lead ions from contaminated water bodies effectively. Composites of HAP containing $CeO_2$ and $La(OH)_3$ were prepared using in situ wet precipitation of HAP, followed by the addition of $Ce(SO_4)_2$ and $La(NO_3)_3$ into the same reaction mixture. The resultant solids were tested for the removal of fluoride and lead ions from contaminated water. It was found that the composite HAP·$CeO_2$ shows fluoride and lead ion removal capacities of 185 and 416 mg/g, respectively. The fluoride removal capacity of the composite was improved when $La(OH)_3$ was incorporated and it was observed that the composite HAP·$CeO_2$·$La(OH)_3$ (3:2) has the highest recorded fluoride removal capacity of 625 mg/g. The materials were characterized using scanning electron microscopy–energy-dispersive X-ray (SEM-EDX) spectrometry, Fourier transform infrared (FT-IR) spectrometry, X-ray powder diffractometry (XRD), X-ray photoelectron spectroscopy (XPS), and Brunauer–Emmett–Teller (BET) surface area analysis. Analysis of results showed that Ce and La are incorporated in the HAP matrix. Results of kinetic and leaching analyses indicated a chemisorptive behavior during fluoride and lead ion adsorption by the composites; meanwhile, the thermodynamic profile shows a high degree of feasibility for fluoride and lead adsorption.

## 1. INTRODUCTION

Toxic elements even with low concentrations in drinking water can be considered as silent killers for both terrestrial and aquatic organisms. Their sources vary, and these can be simple leaching from minerals[1] or due to anthropogenic activities.[2] Of these elements, lead is of major concern as water can get exposed to it frequently.[3−6] On the other hand, nonmetals like fluoride have also been the topic in many issues as it is being identified in connection to chronic kidney disease of unknown etiology (CKDu),[7] dental fluorosis,[8] arthritis,[9] and brittle bone disease.[9]

Hence, the removal of excess fluoride and lead ions from contaminated water systems is an urgent need and has gained much attention from the scientific community. Various approaches[10−18] exist to remove these toxins from water, and adsorption has been the most widely used technique owing to its simplicity and cost effectiveness. However, the high-performance advanced materials that are capable of showing fast and high adsorption capacity toward fluoride and lead ions are yet to be studied. Materials such as lignin,[19] chitosan,[20] cellulose,[20] hydroxyapatite (HAP),[21,22] montmorillonite and kaolinite,[23] fly ash,[23] and natural metal oxides[24] have been broadly studied for the removal of lead ions. The sorbent, HAP, and its composites, namely, HAP-granular activated carbon (GAC),[22] HAP-

Received: December 5, 2020
Accepted: May 3, 2021
Published: May 17, 2021

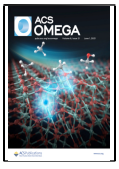

chitosan,[20] and HAP-carboxy methyl cellulose,[20] have exhibited excellent adsorption capacity toward lead ions. Comparatively, a vast variety of materials for fluoride removal have been developed such as activated alumina,[25−27] calcium-based materials,[28,29] iron-based sorbent materials,[30,31] metal oxides,[32,33] carbon-based materials,[32,34] layered double hydroxides,[35,36] and hydroxyapatite.[37,38] Of the advanced materials that have been developed for fluoride removal during the last 2 decades, metal oxides based on rare earth elements such as lanthanum (La(III)), cerium (Ce(IV)), and yttrium (Y(III)) received much attention for fluoride removal. Moreover, the synthesis of lanthanum-modified seaweed,[39] La- and Ce-modified alumina,[40] magnetic core−shell $Fe_3O_4$@Alg-La particles,[41] lanthanum-modified bone waste,[42] lanthanum-impregnated chitosan flakes,[43] and lanthanum oxyhydroxide−GAC hybrid[44] has been reported. Furthermore, the fluoride adsorption behaviors of hydrous Ce(IV)−Zr(IV) oxide,[45] $CeO_2$−$ZrO_2$ nanocages,[46] nonthermal plasma-modified $CeO_2$/Mg−Fe layered double hydroxides,[35] cerium dispersed in carbon,[47] silica-based ceria,[48] and Al−Ce hybrids[49] have been studied.

By evaluating the structure−activity relationship of these composites, it is apparent that the presence of cerium and lanthanum in the composites have contributed to the ballistic adsorption toward fluoride. On the other hand, HAP shows a superior uptake capacity for different metal ions. Hence, the quest for highly advanced materials for lead and fluoride ion adsorption can be fulfilled by incorporating cerium and lanthanum into the HAP matrix.

In this work, the structure of the HAP was tuned to enhance the adsorption of fluoride and lead ions by incorporating cerium and lanthanum ions into the matrix. The in situ wet chemical precipitation method was used to decorate and fabricate HAP with lanthanum and cerium. The decorated surfaces of HAP as well as HAP itself mainly contribute to diminishing these ions via cation exchange, metal complexion, electrostatic interaction, or apatite dissolution.

## 2. RESULTS AND DISCUSSION

**2.1. Formation Mechanism of Lanthanide-Impregnated HAP.** The formation of lanthanide-incorporated HAP is an in situ wet chemical precipitation method. When $(NH_4)_2HPO_4$ and $Ca(NO_3)_2{\cdot}4H_2O$, which are in a 1.67 Ca/P molar ratio, were mixed in the basic medium, the nucleation reaction of calcium and phosphates to produce HAP occurs. At this point, $Ce(SO_4)_2$ and oxygen gas were introduced and the system was maintained in the basic condition (pH = 10). The solubility product ($K_{sp}$) of $Ce(OH)_4$ is $7.8 \times 10^{-51}$, and therefore the pH threshold of $Ce(OH)_4$ is approximately 4 at 27 °C.[50] As the first step, nucleation of $Ce(OH)_4$ takes place, and after forming certain unstable complexes, a $CeO_2$ yellow precipitate will be produced along with hydroxyapatite.[51,52] During lanthanum-incorporated HAP·$CeO_2$ (HC) production, $La(NO_3)_2$ was added with the addition of $Ce(SO_4)_2$ while maintaining the pH at more than 10 as the pH threshold of $La(OH)_3$ is 9.6. Therefore, $La(OH)_3$ nucleation occurs simultaneously with $CeO_2$ as shown in eqs 1 and 2,[24] where $MO^-$ denotes the hydrous ceria or Ca surface groups of hydroxyapatite.

$$POH + La^{3+} + 2OH^- \rightarrow POLa(OH)_2 + H^+ \quad (1)$$

$$MO^- + La^{3+} + 2OH^- \rightarrow MOLa(OH)_2 + H^+ \quad (2)$$

**2.2. Characterization.** The Fourier transform infrared (FT-IR) spectra of the synthesized HAP·$CeO_2$ (HC), HAP·$CeO_2$·$La(OH)_3$ (2:1) (HCL 1), and HAP·$CeO_2$·$La(OH)_3$ (3:2) (HCL 2), given in Figure 1, show broad peaks at 1631, 1625, and

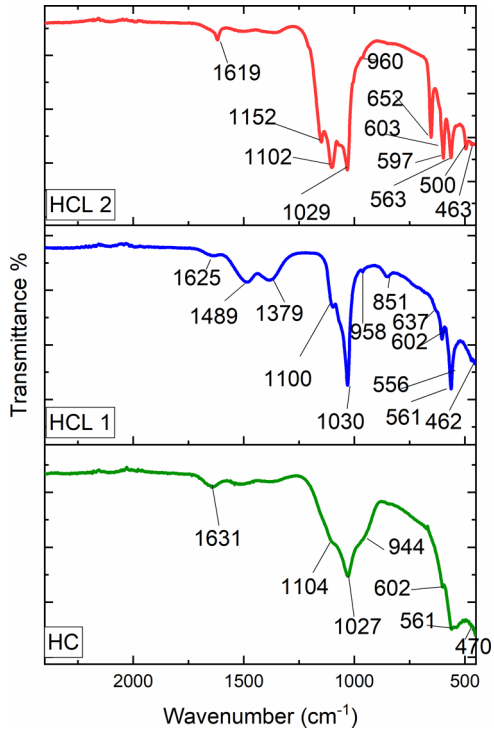


**Figure 1.** FT-IR spectra of synthesized HC, HCL 1, and HCL 2.

1619 $cm^{-1}$, respectively, which indicate the presence of the OH group in adsorbed water.[53−57] The peaks at 603 and 563 $cm^{-1}$ of the HCL 2 spectrum and at 602 and 561 $cm^{-1}$ of the HC and HCL 1 spectra refer to the bending mode of the phosphate (O−P−O) group.[53,58,59] Moreover, the adsorption bands that appeared in the range of 1027−1030 and 1100−1104 $cm^{-1}$ represent the asymmetrical and symmetrical stretching modes of P−O and phosphate.[22,58] In addition, a duplex peak appeared at 1489 and 1379 $cm^{-1}$ of HCL 1, which refers to the carbonate peak, which resulted due to the $CO_2$ adsorption by HAP.[58] The band that appeared in the 450−550 $cm^{-1}$ region can be assigned to the Ce−O stretching vibration.[60−62] Moreover, the adsorption peak observed in the 652 $cm^{-1}$ region in the HCL 2 spectrum and the small peak that appeared in the 637 $cm^{-1}$ region of the HCL 1 spectrum represent the vibrational mode of the La−O bond.[63] These results confirm the successful formation of the HC composite, which consists of HAP and ceria as well as the synthesis of HCL 1 and HCL 2 composites, which comprise HAP, ceria, and $La(OH)_3$.

The microstructure characteristics and chemical composition profiles of composites were measured by scanning electron microscopy (SEM) and energy-dispersive X-ray (EDX) technology (Figures S1−S4). As shown in Figure S1a, the shape of the HC particles is more irregular and the average particle size is approximately 200 nm. Moreover, the morphology of the composite is more similar to the shape of the cerium oxide, which is crystallized in rounded plates.[51] Figure S1b illustrates the morphology of HCL 1, and it clearly shows that the agglomeration of particles and the shape of the particles are more similar to the rod shape of the neat


https://doi.org/10.1021/acsomega.0c05935
ACS Omega 2021, 6, 13527−13543

hydroxyapatite, and the average size of the particles is approximately 70 nm. Figure S1c shows the morphology of the HCL 2 composite, and it clearly indicates the presence of both rod-shaped and rounded-plate-shaped particles with approximately 150 nm average diameter.

Figure S2 shows the surface chemical composition of HC and its elemental distribution. Figure S2a shows the selected portion of the composites for elemental mapping, and Figure S2b,c−f indicates the presence of the Ce element in addition to the unique elements' presence in hydroxyapatite (HAP), such as Ca, P, and O.

Figure S3 illustrates the chemical composition and elemental distribution of the HCL 1 composite. The surface elemental analysis of HCL 1 confirms the presence of cerium and lanthanum on the composite surface (Figure S3b−g).

On the other hand, Figure S4 shows EDX results for the HCL 2 composite, and it clearly indicates that the Ce and La elements are densely distributed on the HCL 2 than HCL 1. The surface distributions of Ce and La on the HCL 2 composite are 31 and 19%, while those values for HCL 1 are 8 and 5%, respectively. This result is in good agreement with the synthesis protocol (which was mentioned in 3.3) as the Ce/La ratio of HCL 2 is higher than the HCL 1 composite.

Figure 2 shows the X-ray diffraction patterns of HC, HCL 1, and HCL 2 composites. It can clearly be seen that the

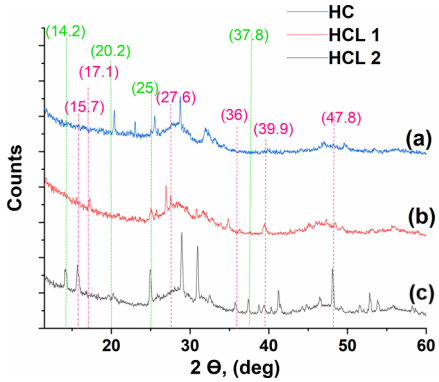


**Figure 2.** X-ray diffraction patterns of (a) HC, (b) HCL 1, and (c) HCL 2.

characteristic and dominant diffraction pattern of HAP persists even after adding $Ce(SO_4)_2$ and $La(NO)_3$ to the reaction mixture. The peaks that appear in the range of 28−34° can be assigned to both $CeO_2$ and HAP.[52,64−66] Furthermore, the diffraction patterns of HCL 1 and HCL 2 composites show almost identical patterns for $La(OH)_3$ and $La_2O_3$, which are denoted at 14.2, 20.2, 25, and 37.8°. However, the presence of the 100 phase at 14.2° confirms the presence of the diffraction signature of $La(OH)_3$ in the composites. These results confirm the formation of the hydroxyapatite/ceria composite and the hydroxyapatite/ceria/lanthanum hydroxide compound.

The lead ion adsorption onto HC, HCL 1, and HCL 2 composites was further confirmed by following the X-ray diffraction (XRD) pattern of lead-adsorbed composites at different time intervals (Figure 3). From these analyses, it was identified the formation of a new phase at the 31.42° region of HC, and it can be attributed to the lead HAP or hydroxypyromorphite (Figure 3a). Moreover, it can clearly be seen the appearance of this phase even after 5 min. As revealed by the kinetic data, the lead and HC composite equilibrated within 6 min. However, an intense peak for the PbHAP was observed after 60 min. Therefore, other than the ion-exchange reaction with a calcium ion, another mechanism, which is hydroxyapatite dissolution, followed by precipitation is involved in the lead ion adsorption process.[67] Once the HC adsorbs lead, the composite will form a $Pb_{(10-x)}Ca_x(PO_4)_6(OH)_2$ complex, which is a highly unstable complex with a high calcium content.[67] As a result, the intermediate complex will be dissolved and precipitate with time by producing a new phase with $Pb_{10}(PO_4)_6(OH)_2$.[67] On the contrary, the diffraction patterns of lead-adsorbed HCL 1 and HCL 2 do not show any diffraction signature for hydroxypyromorphite. Thus, it can be predicted that lead ion adsorption occurs via ion exchange rather than dissolution and precipitation. Moreover, the intensity of the peaks related to the lanthanum-based compound and HAP diminished due to exchange of lanthanum and calcium ion with lead. Moreover, Figure 3b shows the XRD spectra of fluoride-adsorbed HCL 2 composites at different time intervals. The new peak that appeared at 29.7 after 5 min fluoride adsorption onto HCL 2 composites may indicate the formation of a new phase, and it can be attributed to the 002 plane of $LaF_3$ (ICDD 01-075-7706). However, the formation of a new phase related to $CeF_4$ is difficult to distinguish because its characteristic planes coincide with the peaks of HAP and $La(OH)_3$.

X-ray photoelectron spectroscopy (XPS) analysis was conducted to support the adsorption mechanism of $Pb^{2+}$ and $F^-$ with three HAP composites. In this study, wide XPS spectra of HC, HCL 1, and HCL 2 before and after adsorption of $Pb^{2+}$ and fluoride were measured to perform elemental identification as well as quantity of a detected element, which can be estimated using the intensity of the corresponding photoelectron peak in a wide XPS spectrum. It allows the determination of the atomic composition of the selected elements in the sample before and after adsorption.

Figure 4 shows the XPS survey spectra of HC, F-adsorbed HC (F-Ad-HC), and Pb-adsorbed HC (Pb-Ad-HC). The survey spectrum of HC reveals the photoelectron lines and the Auger electron lines from mainly the elemental compositions of Ca, O, P, and Ce and possible surface contamination peaks from C and N in HC composites. The survey spectra of Pb-Ad-HC and F-Ad-HC reveal the photoelectron lines from Pb and F. In the insets of Figure 4 are shown the F 1s and Pb 4f high-resolution XPS spectra measured with a relatively low pass energy (PE) with a high scan number (well-separated spin−orbit components of Pb $4f_{5/2}$ and Pb $4f_{7/2}$ can be observed). This clearly confirms the possibility of adsorbing lead and fluoride ions to the HC.

The Ca/P ratios of neat HC, Pb-Ad-HC, and F-Ad-HC were estimated considering the intensities of photoelectron peaks of Ca 2p and P 2p peaks at binding energies of 347 and 133 eV, respectively. In the estimation process, photoelectron intensities were normalized by the corresponding values of photo-absorption cross sections[68] and inelastic mean free path[69] as given in eq 3.[70−72]

$$\frac{[Ca]}{[P]} = \frac{\sigma_{P\ 2p(h\nu)}\lambda_{p\ 2p\ in\ composites}}{\sigma_{Ca\ 2p(h\nu)}\lambda_{Ca\ 2p\ in\ composites}} \times \frac{I_{Ca\ 2p}}{I_{p\ 2p}} \quad (3)$$

The composition ratios were estimated to be 1.8, 1.7, and 1.8 in the cases of neat HC, Pb-Ad-HC, and F-Ad-HC, respectively. The value of 1.8 is consistent with the reported value of the Ca/P ratio of HAP, and it confirms the successful incorporation of HAP with $CeO_2$ in the in situ preparation without impairing the


https://doi.org/10.1021/acsomega.0c05935
ACS Omega 2021, 6, 13527−13543

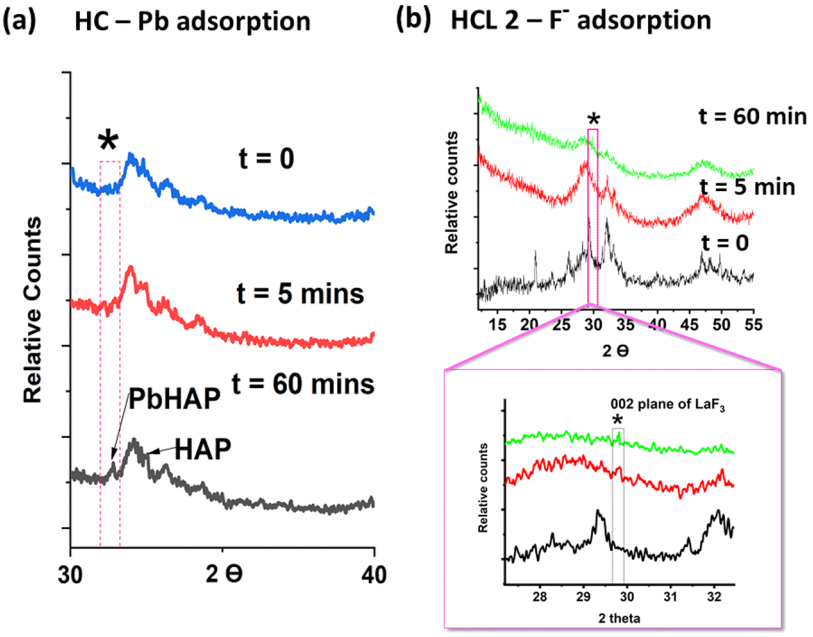


**Figure 3.** XRD diffraction pattern of (a) neat HC and Pb-adsorbed HC after 5 and 60 min and (b) neat HCL 2 and fluoride-adsorbed HCL 2 after 5 and 60 min.

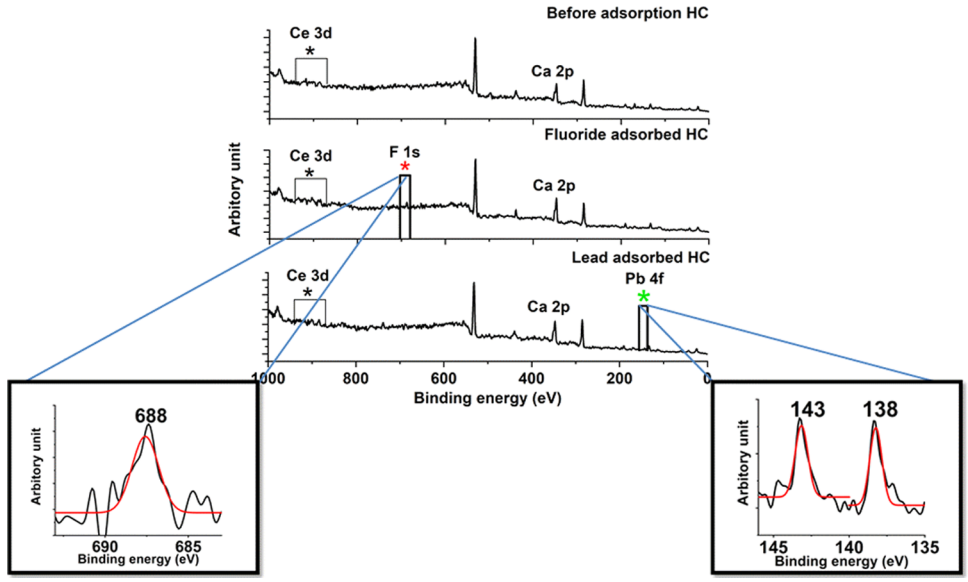


**Figure 4.** XPS spectra of neat HC, F-Ad-HC, and Pb-Ad-HC.

original composition of HAP.[73] In contrast to F adsorption, the composition ratio of Ca/P in HC decreased to 1.7 due to $Pb^{2+}$ adsorption. This result is consistent with the results obtained via the leaching study as Ca ion leaching was found during $Pb^{2+}$ adsorption. Further, the leaching effect was hardly observed during $F^-$ adsorption, which is also consistent with the XPS analysis as the composition ratio of Ca/P did not change over the adsorption of F.

The decrement of the Ca/P ratio via $Pb^{2+}$ adsorption can be attributed to either the removal of the $Ca^{2+}$ ion or both the $Ca^{2+}$ ion and P simultaneously by keeping a constant ratio of 1.7. To examine any removal of P from the HAP structure, Ca/Pb and P/Pb ratios were considered, and the estimated values were approximately 17 and 10, respectively. However observed ratio of Ca/P clearly in agreement with the value corresponding to the removal of $Ca^{2+}$ ions. Thus, it can be concluded that the atomic concentration of P atoms remains constant over the $Pb^{2+}$ adsorption and allows one to confirm that the ion exchange occurred only by the removal of $Ca^{2+}$ during the $Pb^{2+}$ adsorption process. In the mechanism of $Pb^{2+}$ adsorption, it was interpreted by leaching experiments as the adsorption of $Pb^{2+}$ to either the −POH or $-POCa^+$ group via ion exchange with $Ca^{2+}$ or $H^+$ as shown in eqs 4 and 5,[67] and the XPS analysis supports the interpretation of the removal of $Ca^{2+}$ by the adsorption of $Pb^{2+}$.

$$-POCa^+ + Pb^{2+} \rightarrow POPb^+ + Ca^{2+} \quad (4)$$

$$-POH + Pb^{2+} \rightarrow POPb^+ + H^+ \quad (5)$$

In addition, $F^-$ adsorption can occur with Ce atoms as shown in eqs 7−9. However, a considerable change in Ce 3d XPS spectra due to the Ce−F interaction was not observed in the high-



https://doi.org/10.1021/acsomega.0c05935
ACS Omega 2021, 6, 13527−13543

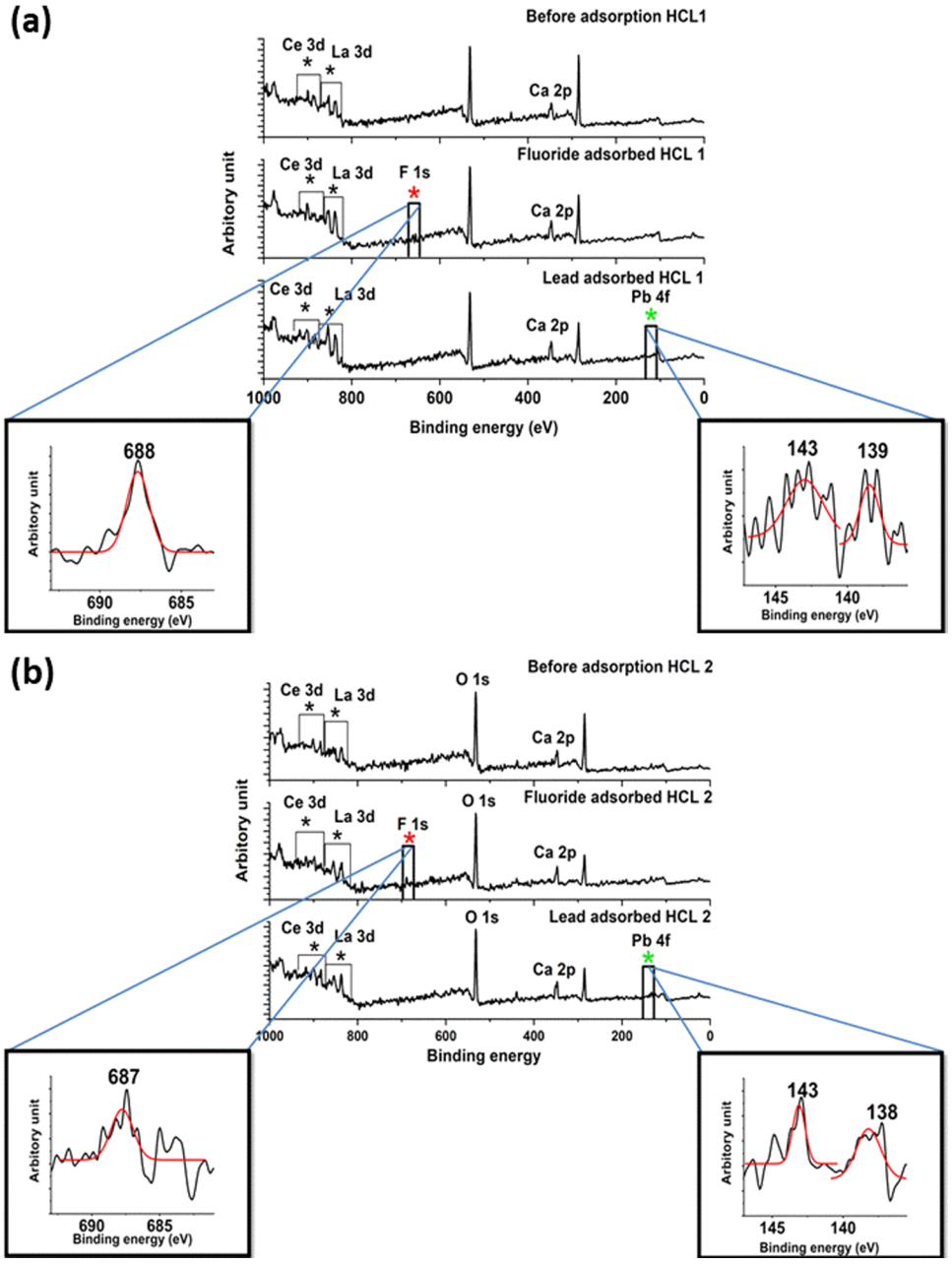


**Figure 5.** XPS wide spectra of (a) HCL 1 and (b) HCL 2.

resolution spectra of Ce 3d, and this may be due to the smaller atomic concentration of adsorbed F atoms as well as the pass energy still being relatively high (resolution was not good enough) for the measurements to obtain such components due to the different chemical states of the Ce 3d level.

The XPS survey spectra that represent HCL 1 and HCL 2 are overlaid in Figure 5. The two broad peaks at 850 and 835 eV with spin−orbital splitting of 15 eV correspond to the La $3d_{5/2}$ and La $3d_{3/2}$, as can be seen in the wide spectra of both HCL 1 and HCL 2, confirming the La incorporation.

In the insets of Figure 5 are shown the F 1s and Pb 4f high-resolution spectra measured with a relatively low pass energy with a high scan number. However, the Pb 4f high-resolution spectra had a poor signal-to-noise ratio compared to $Pb^{2+}$ adsorption on HC, and this might be due to the relatively low Pb adsorption with the existence of La. The adsorption behaviors of $Pb^{2+}$ and $F^{-}$ are discussed considering several composition ratios before and after adsorption.

According to the results obtained via the leaching experiment, it was confirmed that there was an exchange of $Ca^{2+}$ and $La^{3+}$ with $Pb^{2+}$ during $Pb^{2+}$ adsorption. Furthermore, it was obtained that the loading level of La is higher in the HCL 2 composite than the HCL 1 composite. This idea can be confirmed by the following table of composition ratios before and after Pb adsorption estimated from XPS wide spectra of HCL 1 and HCL 2. Considering the composition ratios from Table 1, in the cases of HCL 1 and HCL 2, the atomic concentrations of Ca and La decreased by $Pb^{2+}$ adsorption, where the decrease can be attributed to the removal of $Ca^{2+}$ (eq 4) and $La^{3+}$ (eq 6) by the adsorption of $Pb^{2+}$.

Further, HCL 2 displays a higher adsorption of $Pb^{2+}$; thus, it can be concluded that the XPS results for $Pb^{2+}$ adsorption of HCL 1 and HCL 2 are consistent with the model proposed from


https://doi.org/10.1021/acsomega.0c05935
ACS Omega 2021, 6, 13527−13543

**Table 1. Composition Ratios of HCL 1 and HCL 2 before and after Lead Ion and Fluoride Adsorption**

| $Pb^{2+}$ adsorption | HCL 1 | HCL 2 |
|---|---|---|
| before Ca/P/La | 1.8:1.0:0.52 | 1.7:1:1.2 |
| after Ca/P/La/Pb | 1.26:1.0:0.22:0.04 | 0.9:1.0:0.4:0.06 |
| $F^-$ adsorption | HCL 1 | HCL 2 |
| before Ca/P/La | 1.8:1.0:0.50 | 1.7:1.0:1.2 |
| after Ca/P/La/Pb | 1.8:1.0:0.40:0.7 | 1.7:1.0:1.2:1.3 |

leaching experiments and adsorption isothermal experiments. Also, it is observed considering the significant decrease in the Ca/P ratio of HCL 1 and 2 compared to HC over $Pb^{2+}$ adsorption, suggesting the higher possibility of removal of the $Ca^{2+}$ ion in the existence of La in both composites by the adsorption of $Pb^{2+}$. In addition, the higher adsorption of $Pb^{2+}$ in HCL 2 can be attributed to the existence of a relatively higher atomic concentration of La in HCL 2, where the degree of existence of La may influence the degree of absorption of $Pb^{2+}$ as well as the removal process of $Ca^{2+}$.

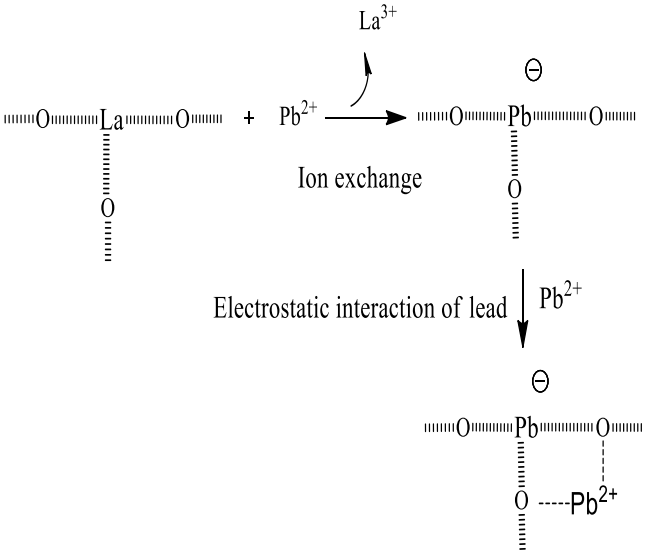


On the other hand, in the case of F adsorption, Ca/P/La ratios remain constant by fluoride adsorption for both HLC 1 and HCL 2, as shown in Table 1. Thus, it can be concluded that the removal of $Ca^{2+}$ and $La^{3+}$ ions is not possible over the adsorption of $F^-$, as was also suggested through the leaching experiment results. Also, it is clear that HCL 2 displayed a higher adsorption of $F^-$ considering the composition ratios in Table 1. The mechanism of fluoride adsorption onto these composites is shown in eqs 7–9, where M denotes the Ca, Ce, or La surface groups of composites.

$$-MOH_2^+ + F^- \xrightarrow{\text{electrostatic interaction}} -MOH_2 \cdots F \quad (7)$$

$$-MOH_2^+ + F^- \xrightarrow{\text{water replacement}} -MF + H_2O \quad (8)$$

$$-MOH + F^- \xrightarrow{OH^- \text{ replacement}} -MF + OH^- \quad (9)$$

In the XRD results, HCL 2 displays a peak related to $LaF_3$, confirming the formation of La−F during fluoride adsorption for HCL 2. This is because HCL 2 shows a higher adsorption of F compared to HCL 1 and HC. Also, it allows suggesting that the existence of La may have an influence on obtaining a higher degree of adsorption of $F^-$ to the composites via the formation of La and F (eqs 8 and 9).

Moreover, the chemical composition profiles of three different composites obtained from XPS and EDX analyses were compared and are shown in Table S1. A significant correlation between two profiles was not identified, and this is due to the different capabilities, limitations, and depth of analyses of these two instruments.[74]

To better understand the variation of surface area, pore volume, and average pore radius with the adsorption of lead and fluoride ions, Brunauer−Emmett−Teller (BET) analyses were performed before and after the adsorption (Figures S5–S7). In this case, multipoint BET analyses as well as the main pore-size distribution using the Barrett−Joyner−Halenda (BJH) method were performed. As shown in Table 2, the surface areas of neat HC, HCL 1, and HCL 2 were 66.88, 108.58, and 123.67 $m^2/g$, respectively, and after fluoride adsorption, the values decreased to 59.85, 97.74, and 127.31 $m^2/g$, respectively. In addition, the average pore sizes of HC, HCL 1, and HCL 2 also decreased from 4.08, 2.51, and 3.22 nm to 3.72, 2.35, and 3.04 nm upon the adsorption of $Pb^{2+}$. Therefore, these pieces of evidence clearly demonstrate the accumulation of $Pb^{2+}$ in the pores of the adsorbent. On the other hand, fluoride adsorption to these composites again shows a pattern similar to that of lead ion adsorption, i.e., the average pore size of the composite reduced upon $F^-$ adsorption. However, the pattern that changes the surface area is different in the fluoride-adsorbed composites than lead ion adsorbed composites. In this case, F-Ad HCL 2 and F-Ad HC show increment of surface area while F-Ad HCL 1 shows decrement in surface area.

Figure 6 shows the fluoride adsorption experimental data that fitted to the Langmuir and Freundlich isotherm models. The parameters of isotherms are given in Table 3. These results explain that the adsorption process of HC at equilibrium is in better agreement with the Freundlich adsorption isothermal

**Table 2. Calculated Data of Surface Area and Average Pore Size Using Multipoint BET Analysis and BJH Analysis**

| multipoint BET analysis | | | | | | | | | |
|---|---|---|---|---|---|---|---|---|---|
| parameter | | HC | HC-F | HC-Pb | HCL 1 | HCL 1-F | HCL 1-Pb | HCL 2 | HCL 2-F | HCL 2-Pb |
| surface area ($m^2/g$) | | 66.88 | 102.85 | 59.85 | 108.58 | 93.10 | 97.74 | 123.67 | 127.91 | 127.31 |
| average pore size (nm) | | 4.08 | 3.58 | 3.72 | 2.51 | 2.36 | 2.35 | 3.22 | 3.05 | 3.04 |
| BJH analysis | | | | | | | | | | |
| parameter | | HC | HC-F | HC-Pb | HCL 1 | HCL 1-F | HCL 1-Pb | HCL 2 | HCL 2-F | HCL 2-Pb |
| surface area ($m^2/g$) | A | 28.69 | 51.40 | 25.60 | 24.57 | 22.07 | 27.02 | 42.13 | 54.89 | 37.79 |
| | D | 30.77 | 50.47 | 26.70 | 27.52 | 23.61 | 25.81 | 45.84 | 53.94 | 37.79 |
| average pore size (nm) | A | 1.89 | 1.89 | 1.69 | 1.69 | 1.70 | 1.69 | 1.69 | 1.69 | 1.90 |
| | D | 1.89 | 1.88 | 1.89 | 1.90 | 1.88 | 1.69 | 1.89 | 1.70 | 1.90 |



https://doi.org/10.1021/acsomega.0c05935
ACS Omega 2021, 6, 13527−13543

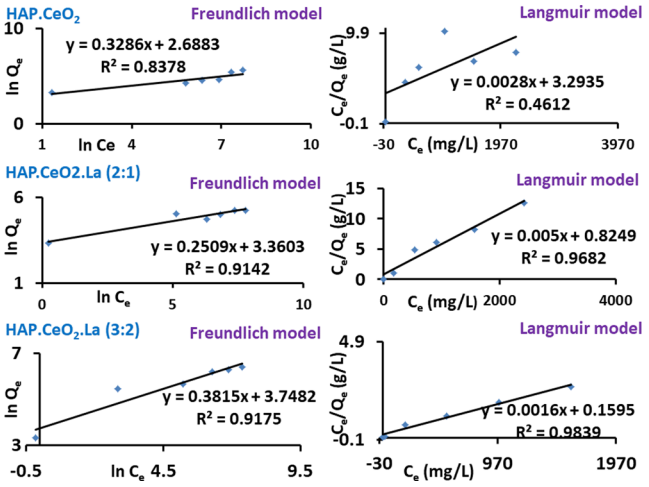


**Figure 6.** Sorption isotherms (Freundlich and Langmuir models) for fluoride adsorption onto HC, HCL 1, and HCL 2.

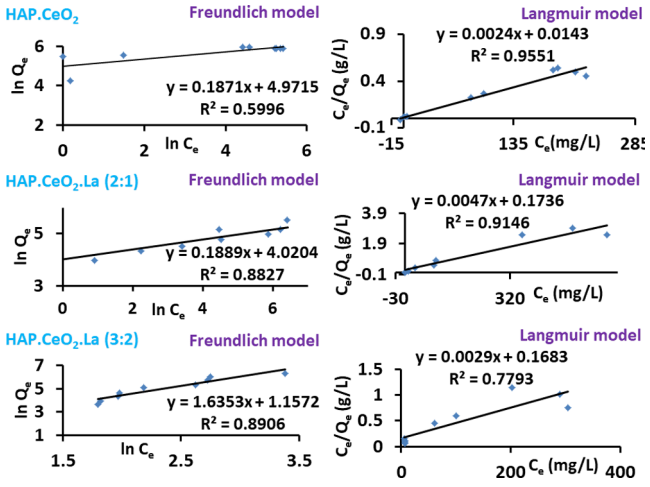


**Figure 7.** Sorption isotherms (Freundlich and Langmuir model) for lead ion adsorption onto HC, HCL 1, and HCL 2.

model. Thus, it reveals that the adsorption process at equilibrium occurs on a heterogeneous surface and therefore binding sites of HC for fluoride ions are not energetically equivalent. Comparatively, the equilibrium adsorption processes of HCL 1 and HCL 2 are in good agreement with the Langmuir model, and it reveals the monolayer adsorption of fluoride at the equilibrium. According to these results, the fluoride adsorption capacities of HC, HCL 1 and HCL 2 are 185.2, 200, and 625 mg/g, respectively.

Figure 7 shows the lead ion adsorption experimental data that fitted the Langmuir and Freundlich isotherm models. The parameters of isotherms are given in Table 3. The lead ion adsorption experimental data of HC and HCL 1 nicely agree with the Langmuir model. However, the lead ion adsorption data of HCL 2 show a better agreement with the Freundlich model, indicating the multilayer adsorption of lead. According to these results, the lead ion adsorption capacities of HC, HCL 1 and HCL 2 are 416, 213, and 296 mg/g, respectively.

**2.3. Adsorption Isotherm Comparison.** As described in the batch adsorption experiment, sorption isotherms such as Langmuir and Freundlich were used to determine the maximum adsorption capacity and linear regression coefficients were used to determine the best-fitting isotherm. However, the comparison of linear regression values as a sole criterion to identify the

**Table 3. Isotherm Parameters for Fluoride and Lead Ion Adsorption by HC, HCL 1, and HCL 2**

| isotherm parameters | | $F^-$ adsorption HC | $Pb^{2+}$ adsorption HC |
|---|---|---|---|
| experimental data | $q_e$ (mg/g) | 285.0 | 427.7 |
| Langmuir model | $q_e$ (mg/g) | 322.6 | 416.0 |
| | $K_1$ ($min^{-1}$) | 0.2 | 0.2 |
| | $R^2$ | 0.4612 | 0.9551 |
| Freundlich model | $q_e$ (mg/g) | 185.2 | 357.0 |
| | $K_f$ (g/(mg min)) | 2.3 | 2.3 |
| | $R^2$ | 0.8378 | 0.5996 |
| | $n$ | 1.5 | 0.2 |
| isotherm parameters | | $F^-$ adsorption HCL 1 | $Pb^{2+}$ adsorption HCL 1 |
| experimental data | $q_e$ (mg/g) | 191.0 | 191.0 |
| Langmuir model | $q_e$ (mg/g) | 200.0 | 212.8 |
| | $K_1$ ($min^{-1}$) | 0.17 | 0.17 |
| | $R^2$ | 0.9682 | 0.9682 |
| Freundlich model | $q_e$ (mg/g) | 111 | 187.8 |
| | $K_f$ (g/(mg min)) | 2.3 | 2.3 |
| | $R^2$ | 0.9142 | 0.9146 |
| | $n$ | 1.5 | 5.3 |
| isotherm parameters | | $F^-$ adsorption HCL 2 | $Pb^{2+}$ adsorption HCL 2 |
| experimental data | $q_e$ (mg/g) | 605.0 | 406.0 |
| Langmuir model | $q_e$ (mg/g) | 625.0 | 5.90 |
| | $K_1$ ($min^{-1}$) | 0.2 | $2.8 \times 10^{-8}$ |
| | $R^2$ | 0.9839 | 0.7793 |
| Freundlich model | $q_e$ (mg/g) | 290.4 | 296.0 |
| | $K_f$ (g/(mg min)) | 2.3 | 28.6 |
| | $R^2$ | 0.9175 | 0.844 |
| | $n$ | 1.5 | 2.5 |



https://doi.org/10.1021/acsomega.0c05935
ACS Omega 2021, 6, 13527−13543

appropriate isotherm model is not enough, and experimental data is also needed for analysis employing the $X^2$ test. The statistic $X^2$ test, which is the sum of squares of the difference between the experimental adsorption capacity and the calculated adsorption capacity divided by the corresponding calculated adsorption capacity value, is shown in eq 10.[75,76]

$$X^2 = \sum \frac{[q_{e,exp} - q_{e,cal}]^2}{q_{e,cal}} \quad (10)$$

where $q_{e.exp}$ (mg/g) is the experimental adsorption capacity at equilibrium and $q_{e,cal}$ (mg/g) is the calculated adsorption capacity at equilibrium. Generally, $X^2$ increases on increasing the deviation between calculated and experimental adsorption capacities.

The summary of the statistic $X^2$ test and linear regression coefficient parameters is given in Table S2. Based on these data, it can be directly proposed that the Langmuir model is the best-fitting model for HC-based lead ion adsorption. Also, the lead adsorption statistic data of the HCL 1 composite shows a less significant difference between the Langmuir model and the Freundlich model. However, as described earlier, the XPS data of lead ion adsorbed HCL 1 and leaching studies of lanthanum and calcium during lead adsorption support more the Langmuir model rather than the Freundlich model. The Langmuir model exhibited a lower $X^2$ value and a higher regression coefficient value toward HCL-2-based lead ion adsorption than the Freundlich model. When $F^-$ adsorption onto HC is considered, the statistic $X^2$ test exhibits a lower $X^2$ value for the Langmuir model. However, that model exhibits a lower regression coefficient value and that indicates that the Freundlich isotherm model is the best model for fluoride adsorption. With a higher linear regression coefficient and lower $X^2$ values, the Langmuir adsorption isotherm model appeared to be the best fit for HCL-2- and HCL-1-based fluoride adsorption.

**2.4. Influence of pH on Fluoride and Lead Uptake Capacity.** Figure 8 exhibits the variation of fluoride and lead ion adsorption capacity with pH of the medium. The influence of pH on lead ion adsorption was monitored in the range of 1−6 using 0.02 g/10 mL 150 ppm lead ion solution. The pH threshold of lead hydroxide is approximately 6 at 27 °C, and once the pH of the system exceeds the pH threshold value, both precipitation and adsorption processes contribute to reducing the $Pb^{2+}$ in the medium. Hence, to exclude the effect of lead hydroxide precipitation, the experiment was conducted in the range of 1−6. According to Figure 8a, the optimum pH range of lead ion adsorption is 3−6. The pH threshold of the $La(OH)_3$ precipitate is around 9.6 at 27 °C ($K_{sp} = 2 \times 10^{-21}$), and therefore at lower pH values, the solubility of $La(OH)_3$ increases; consequently, the $La^{3+}$ ion concentration in the medium increases. Moreover, at very low pH values, dissolution of HAP also occurs and it may lead to an increase in the calcium ion concentration in the medium. Therefore, the competition from $La^{3+}$ and $Ca^{2+}$ and the unavailability of a stable surface lead to a decrease in the lead ion adsorption capacity at low pH values.

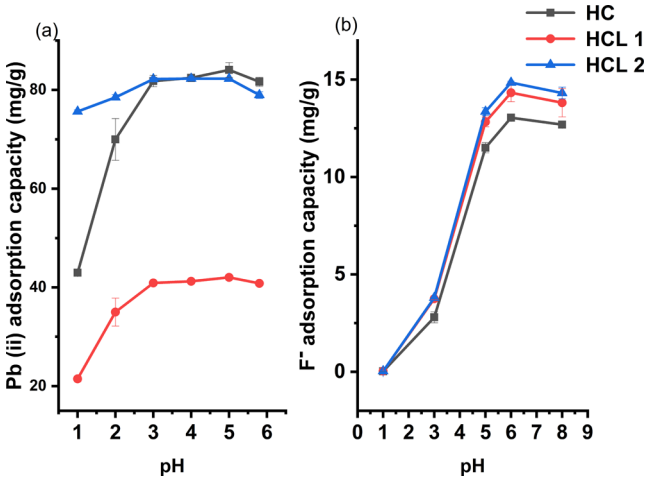


**Figure 8.** Variation of adsorption capacity with pH: (a) lead ion adsorption capacity variation with pH; (b) fluoride adsorption capacity variation with pH.

Figure 8b shows the variation of fluoride adsorption capacity in the range of 1−8. It could be clearly observed that the maximum fluoride adsorption capacity lies in the pH 5−6 region. Due to the HAP dissolution at low pH values, anions such as phosphate hydroxides release into the medium. This competition coming from coexisting anions leads to a decrease in the fluoride adsorption capacity.

**2.5. Thermodynamic and Adsorption Kinetic Studies.** The kinetic parameters, significant differences between experimental and calculated adsorption capacities, and the correlation coefficient at three different temperatures are listed in Table 4. As could be observed, the kinetic profile of lead ion adsorption onto lanthanide incorporated hydroxyapatite shows higher linear regression coefficient values and lower $X^2$ values with the pseudo-second-order kinetic model, indicating that the pseudo-second-order kinetic model is the best model to explain lead ion adsorption onto all three systems. Generally, the pseudo-second-order kinetic model is used to describe adsorption processes, where chemisorption between the adsorbate and adsorbent is the rate-limiting step. These results confirm the previously suggested mechanisms of lead ion adsorption such as ion exchange and precipitation after lead ion adsorption. Although the suitable lead ion adsorption model for lanthanide-incorporated hydroxyapatite was easily identified, the insight of fluoride adsorption is a little complex.

When fluoride adsorption onto HC is considered, the Lagergren-first-order model shows a higher regression coefficient value ($R^2$: 0.9898, 0.9926, and 0.9876 at 27, 50, and 60 °C, respectively) with higher $X^2$values ($X^2$: 0.90, 7.07, and 1.98 at 27, 50, and 60 °C, respectively) compared to the pseudo-second-order kinetic model ($R^2$: 0.9634, 0.9673, and 0.9443; $X^2$: $1.03 \times 10^{-5}$, $2.60 \times 10^{-4}$, and $3.30 \times 10^{-3}$ at 27, 50, and 60 °C, respectively). However, the appearance of lower significance difference between experimental and calculated adsorption capacities at three different temperatures strongly suggests the pseudo-second-order kinetic model as the best correlation model for the kinetic data of fluoride ion adsorption onto HC. On the other hand, the linearized regression coefficient value of the pseudo-second-order kinetic model is also in the acceptable region. The best correlation model for the kinetic data of fluoride ion adsorption onto HCL 1 was obtained with the second-order kinetic model ($R^2$: 0.9753, 0.9425, and 0.9773; $X^2$: $5.7 \times 10^{-4}$, $1.3 \times 10^{-4}$, and $2.32 \times 10^{-6}$ at 27, 50, and 60 °C, respectively). Therefore, it can be concluded that the chemisorption processes such as metal fluoride complexation as depicted in eqs 8 and 9 determine the rate-limiting steps of HCL 1 during fluoride adsorption. As shown in Table 4, the regression coefficient values as well as $X^2$ values of fluoride


https://doi.org/10.1021/acsomega.0c05935
ACS Omega 2021, 6, 13527−13543

**Table 4. Kinetic Parameters and Significance Difference Values of the Lagergren-First-Order Model and Pseudo-Second-Order Kinetic Models for Adsorption of $F^-$ and $Pb^{2+}$ onto Lanthanide-Incorporated Hydroxyapatites**

| | | $F^-$ adsorption | | | $Pb^{2+}$ adsorption | | |
|---|---|---|---|---|---|---|---|
| | | 27 °C | 50 °C | 60 °C | 27 °C | 50 °C | 60 °C |
| HC—Lagergren-first-order model | exp. $q_e$ | 1.55 | 1.50 | 1.49 | 222.38 | 222.37 | 222.39 |
| | $q_e$ (mg/g) | 0.73 ± 0.07 | 0.23 ± 0.01 | 0.5 ± 0.07 | 1.51 ± 0.33 | 0.81 ± 0.06 | 0.33 ± 0.18 |
| | $K_1$ ($min^{-1}$) | 0.59 ± 0.13 | 0.65 ± 0.07 | 0.70 ± 0.01 | 0.21 ± 0.05 | 0.29 ± 0.07 | 0.074 ± 0.07 |
| | $R^2$ | 0.9898 | 0.9926 | 0.9876 | 0.5542 | 0.1485 | 0.4995 |
| | $X^2$ | 0.90 | 7.07 | 1.98 | $2.08 \times 10^5$ | $4.21 \times 10^4$ | $4.27 \times 10^4$ |
| HC—Ho's pseudo-second-order model | $q_e$ (mg/g) | 1.55 ± 0.005 | 1.53 ± 0.007 | 1.48 ± 0.003 | $(222.22 \pm 3.48) \times 10^{-14}$ | $(222.22 \pm 3.48) \times 10^{-14}$ | $(222.22 \pm 3.48) \times 10^{-14}$ |
| | $K_1$ ($min^{-1}$) | 2.13 ± 0.1 | 3.32 ± 0.07 | 10.32 ± 0.87 | 0.51 ± 0.1 | 1.01 | 3.37 ± 0.58 |
| | $R^2$ | 0.9634 | 0.9673 | 0.9443 | 0.8848 | 0.9433 | 0.9043 |
| | $X^2$ | $1.03 \times 10^{-5}$ | $2.60 \times 10^{-4}$ | $3.30 \times 10^{-3}$ | $1.15 \times 10^{-4}$ | $1.01 \times 10^{-4}$ | $1.30 \times 10^{-4}$ |
| HCL 1—Lagergren-first-order model | exp. $q_e$ | 1.56 | 1.63 | 1.73 | 141.6 | 154.36 | 167.95 |
| | $q_e$ (mg/g) | 0.34 ± 0.19 | 0.18 ± 0.05 | 0.11 ± 0.07 | 47.15 ± 1.15 | $(9.13 \times 10^{15}) \pm 2.80$ | $(7.90 \times 10^8) \pm 8.03$ |
| | $K_1$ ($min^{-1}$) | 0.57 ± 0.1 | 1.12 ± 0.2 | 0.87 ± 0.7 | 0.03 ± 0.004 | 2.85 ± 0.021 | 2.69 ± 0.120 |
| | $R^2$ | 0.9867 | 0.9895 | 0.974 | 0.601 | 0.6841 | 0.4613 |
| | $X^2$ | 4.3 | 17.79 | 36.92 | 189.2 | $9.13 \times 10^{15}$ | $7.90 \times 10^8$ |
| HCL 1—Ho's pseudo-second-order model | $q_e$ (mg/g) | 1.59 ± 0.2 | 1.65 ± 0.03 | 1.72 ± 0.001 | 106.38 ± 0.01 | 138.89 ± 1.13 | 172.41 ± 3.00 |
| | $K_1$ ($min^{-1}$) | 3.52 ± 0.1 | 14.29 ± 0.5 | 26.05 ± 6 | 0.07 ± 0.660 | 0.05 ± 0.001 | 0.03 ± 0.005 |
| | $R^2$ | 0.9753 | 0.9425 | 0.9773 | 0.8848 | 0.9433 | 0.7519 |
| | $X^2$ | $5.70 \times 10^{-4}$ | $1.30 \times 10^{-4}$ | $2.32 \times 10^{-6}$ | 11.66 | 1.72 | 0.115 |
| HCL 2—Lagergren-first-order model | exp. $q_e$ | 1.59 | 1.63 | 1.71 | 141.6 | 193.6 | 218.36 |
| | $q_e$ (mg/g) | 0.17 ± 0.01 | 0.041 ± 0.06 | $(0.007 \pm 6) \times 10^{-4}$ | 27.16 ± 1.7 | $(6.95 \times 10^{10}) \pm 3.2$ | 341.17 ± 0.8 |
| | $K_1$ ($min^{-1}$) | 0.51 ± 0.02 | 0.75 ± 0.25 | 0.76 ± 0.17 | 0.10 ± 0.008 | 1.59 ± 0.004 | 1.12 ± 0.2 |
| | $R^2$ | 0.9466 | 0.9399 | 0.9415 | 0.7233 | 0.8557 | 0.6723 |
| | $X^2$ | 12.02 | 61.89 | 420.37 | 482.2 | $6.95 \times 10^{10}$ | 44.2 |
| HCL 2—Ho's pseudo-second-order model | $q_e$ (mg/g) | 1.58 ± 0.006 | 1.64 ± 0.07 | 1.71 | 125 ± 0.9 | 175.43 | 217.39 |
| | $K_1$ ($min^{-1}$) | 5.79 ± 0.4 | 22.24 ± 2.5 | 163.1 ± 4.3 | 0.13 ± 0.01 | 0.32 ± 0.09 | 0.26 ± 0.02 |
| | $R^2$ | 0.9882 | 0.9673 | 0.9807 | 0.9495 | 0.9067 | 0.9688 |
| | $X^2$ | $1.07 \times 10^{-4}$ | $2.44 \times 10^{-6}$ | 0 | 2.20 | 1.88 | 0.004 |



https://doi.org/10.1021/acsomega.0c05935
ACS Omega 2021, 6, 13527−13543

adsorption onto HCL 2 at three different temperatures are in accordance with the pseudo-second-order kinetic model. Hence, it can be concluded that the adsorption of fluoride onto HCL 2 was controlled by a chemical reaction and the type of the chemical reaction is a metal fluoride complexion reaction with water replacement or $OH^-$ replacement. In addition, Figures 9, S8, and S9 show the effect of temperature on the sorption rates of lead and fluoride ions onto HC, HCL 1, and HCL 2. As shown in Figure 9, the time taken to reach equilibrium during fluoride adsorption onto HC is 4 min at 27 °C and 3 min at 50 °C and that of lead adsorption is less than 30 s at 27 °C.

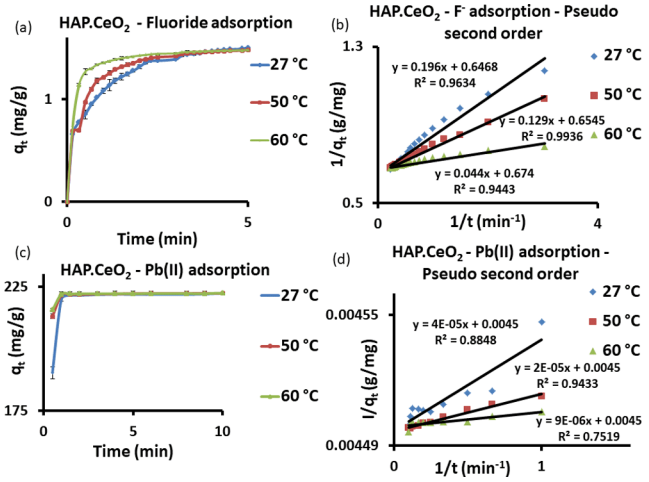


**Figure 9.** Effect of temperature on the sorption rate of and fluoride ions onto HC. (a) Amount of fluoride-adsorbed vs time at different temperatures (HC dosage: 0.2 g/30 mL, at 180 rpm, pH = 5.8). (b) Pseudo-second-order kinetic model at three different temperatures for $F^-$ adsorption. (c) Amount of Pb(II)adsorbed vs time at different temperatures (HC dosage: 0.025 g/10 mL, at 180 rpm, pH = 5.8). (d) Pseudo-second-order kinetic model at three different temperatures for Pb(II) adsorption.

Also, the HCL 1 composite requires 5 and 2 min equilibrium time periods to reach equilibrium at 27 and 50 °C, respectively, and that value for lead adsorption is 25 min at 27 °C and 30 s at 60 °C (Figure S8). As depicted in Figure S9, the time taken to reach equilibrium during fluoride adsorption onto HCL 2 is 4 min at 27 °C and 1.5 min at 50 °C and that value for lead adsorption is less than 10 min at 27 °C and less than 5 min at 60 °C. From this, it could be clearly seen that the sorption rate increases with an increase in temperature. The temperature-dependent nature of the rate constant and the activation energy barrier for sorption were evaluated using the Arrhenius activation energy equation (eq 16). Using the thermodynamic eqs 17−20, plots of ln $K_d$ vs $1/T$ (van't Hoff plot) and ln $k_{ap}$ vs $1/T$ graphs (Arrhenius activation energy plot) were drawn and are shown in Figure S10. The heats of enthalpy and entropy of the system were directly calculated using the slope and intercept of the van't Hoff plot. Moreover, the activation energy barrier for $Pb^{2+}$ and fluoride adsorption was calculated using the slope of the Arrhenius activation energy plot. The calculated thermodynamic parameters and activation energy of the sorption are listed in Table 5. Except for HCL 1, all of the other apparent activation energies ($E_{ap}$) calculated using the Arrhenius equation for fluoride and lead ion adsorption by lanthanide-incorporated hydroxyapatite are positive potentials. Increasing the temperature leads to an increase in the number of adsorbate and adsorbent, which passes the transition potential and thereby increases the rate of adsorption at a given time.

**Table 5. Thermodynamic Parameters for the Adsorption of Fluoride and Lead Ions by Lanthanide-Incorporated Hydroxyapatite**

| | $T$ (K) | $\Delta G°$ (kJ/mol) | $\Delta H°$ (kJ/mol) | $\Delta S°$ (J/(K mol)) | activation energy (kJ/mol) |
|---|---|---|---|---|---|
| | | | $F^-$ Adsorption | | |
| HC | 300 | −0.18 | 20.0 | 66.23 | 35.0 |
| | 323 | −0.24 | | | |
| | 333 | −2.92 | | | |
| HCL 1 | 300 | −0.33 | 44.3 | 148.14 | 50.2 |
| | 323 | −3.06 | | | |
| | 333 | −5.47 | | | |
| HCL 2 | 300 | −0.57 | 55.2 | 184.53 | 76.8 |
| | 323 | −3.10 | | | |
| | 333 | −7.31 | | | |
| | | | $Pb^{2+}$ Adsorption | | |
| HC | 300 | −20.96 | 30.24 | 168.4 | 38.8 |
| | 323 | −21.66 | | | |
| | 333 | −27.72 | | | |
| HCL 1 | 300 | 1.60 | 20.78 | 63.63 | −1.0 |
| | 323 | 0.54 | | | |
| | 333 | −0.65 | | | |
| HCL 2 | 300 | 1.2 | 81.27 | 265.0 | 4.1 |
| | 323 | −2.39 | | | |
| | 333 | −8.50 | | | |

On the other hand, the thermodynamic data reveals that the adsorption of lead ion onto HC is highly favorable compared to the HCL 1 and HCL 2 systems. The $\Delta G°$ value of HC for lead ion adsorption at room temperature (300 K) is −20.96 kJ/mol, while the values for HCL 1 and HCL 2 systems are 1.6 and 1.2 kJ/mol, respectively. Also, all three systems show a high degree of feasibility upon increasing the temperature, indicating the endothermic nature of the lead ion adsorption. Additionally, entropy changes of the systems were also positive, indicating the high randomness at solid−solution interfaces.

According to these thermodynamic parameters, it can be concluded that incorporation of lanthanum ions to HC decreases the affinity toward the lead ion. This observation can be explained via the occupation of anionic active functional groups of HC with lanthanum and the insufficiency of existing functional groups for complete saturation with lead ions. However, the observed $\Delta G°$ values of HCL 1 and HCL 2 are not remarkably high and the activation energies for lead ion adsorption (−1 and 4.1 kJ/mol, respectively) are significantly low, indicating the favorable adsorption even at room temperatures.

**2.6. Effect of Coexisting Ions on Adsorption.** The effect of coexisting anions on fluoride removal was studied in the presence of anions such as $SO_4^{2-}$ (100 ppm), $Cl^-$ (100 ppm), $HCO_3^-$ (100 ppm), and $NO_3^-$ (100 ppm), and it is shown in Figure S11. The results indicated that the presence of this coexisting ion introduces a certain competition on the fluoride adsorption process. The most remarkable effect for fluoride removal can be seen in the HC system, and it is 56.9%. The lowest effect could be seen on HCL 2 (5.9%). It can be explained as the oxidation state of lanthanum is high (+3) and therefore the degree of affinity toward anions is high. Thus, the detrimental effect of the coexisting ion will be lowered. The effect of coexisting cations on $Pb^{2+}$ removal was studied in the


https://doi.org/10.1021/acsomega.0c05935
ACS Omega 2021, 6, 13527−13543

presence of other cations such as $Cd^{2+}$ (100 ppm), $Ca^{2+}$ (100 ppm), and $Mg^{2+}$ (100 ppm) (Figure S12). The lowest effect from the coexisting ion was observed in the HC system, and it is 1.9%. This may be due to the presence of more available surface-active groups on the HC for $Pb^{2+}$ other than the lanthanum-incorporated composites.

**2.7. Leaching Study.** The leaching properties of HC, HCL 1, and HCL 2 during the lead and fluoride ion adsorption process were studied using two different concentrations of lead and fluoride ions. In this case, a 10 mL portion of each concentration was added into 0.02 g of composites, and the leaching of calcium, cerium, and lanthanum ions was determined at different time intervals using microwave plasma atomic emission spectrometry (MP-AES). In this case, the considerable detachment of cerium, lanthanum, and calcium ions during the fluoride adsorption process was not observed. The leaching properties of HC, HCL 1, and HCL 2 during lead ion adsorption are shown in Figure S13. This result indicated that the leaching effect of cerium is zero from each composite even in the presence of 100 ppm lead ion solution. The pH threshold of $CeO_2$ is 2.5 ($K_{sp} = 5.01 \times 10^{-60}$),[77] and therefore at pH values higher than 2.5, $CeO_2$ will not be dissolved and its release to the medium is negligible. By contrast, significant leaching of calcium and lanthanum ions was observed during lead ion adsorption from HCL 1 and HCL 2 at high lead ion concentration (100 ppm). The high lanthanum leaching potential at a high lead ion concentration is a drawback of HCL 1 and HCL 2 composites.[78] However, leaching of lanthanum and calcium ions from HCL 1 and HCL 2 at 1 ppm initial lead ion concentration was not significant, and those values were below the maximum permissible concentrations of calcium (<60 ppm) and lanthanum (<10 ppb).[79] Therefore, by analyzing these results, it can be concluded that HCL 1 and HCL 2 composites are more suitable for customized fluoride removal filters, while the HC composite is suitable for both fluoride and lead ion removal purposes.

**2.8. Point of Zero Charge and ζ Potential of the Composite at pH 5.8.** As suggested in the mechanism, fluoride and lead ion adsorption mainly occurs through the ion-exchange process. The materials consist of strong positively and negatively charged ions, which can facilitate electrostatic interactions of both lead and fluoride ions. Even though the surface charge is not an accurate index to judge the electrostatic interaction of this multivalent and multi-ion versatile material, the surface charge can influence and provide insights into some interactions. To confirm this idea, the point of zero charge ($pH_{pzc}$), where the electrical charge density on the surface is zero, was detected and it provided valuable information regarding the surface charge of the adsorbent. In this case, the graph plotted against ΔpH [$pH_{initial} - pH_{final}$] vs $pH_{initial}$ is shown in Figure S14. The point of zero charge ($pH_{pzc}$) values of HC, HCL 1, and HCL 2 were 5.9 (±0.28), 5.85 (±0.14), and 6.18 (±0.17), respectively. The $pH_{pzc}$ values of all three materials were found to be slightly higher in pH than the working pH of the medium (pH = 5.8), and therefore the surface of the material can exhibit a slight positive charge, which favors the formation of electrostatic interactions with fluoride. Lead adsorption studies carried out in the pH range 1−6 showed a significant lead ion adsorption in the pH range 5−6. This disclosed that lead ion removal is not significantly affected by having this slight positive surface charge. Further, leaching experiments and XPS studies carried out before and after the lead ion adsorption also exhibited sufficient evidence to prove the ion-exchange mechanism of lead ions. Accordingly, lead ion removal was mainly due to electrostatic interactions between lead ion and negatively charged ions such as phosphates in the composite.

The ζ potential in general represents the physical stability of the colloidal suspension, and it gives an idea about the potential difference between the mobile dispersion medium and the electric double layer attached to the dispersed phase.[80] Therefore, the pH of the medium highly affects the ζ potential. In this study, the ζ potentials of three materials at pH 5.8 (working pH) were measured and are shown in Figure S15. From that, it was found that the ζ potentials of HC, HCL 1, and HCL 2 at that pH are positive and that the values are 2.7, 9.3, and 10.4 mV, respectively.[80] According to this, the electrostatic repulsion between two colloidal particles is low and this will lead to further aggregation of particles via the van der Waals interparticle attraction.

**2.9. Straw Filter Experiment.** As shown in Figure 10, a straw filter was developed using a 2 cm nylon rod and tested for fluoride adsorption using HCL 2 (0.2 g) and lead adsorption using HC (0.2 g). The suction filtration studies were carried out until the remaining fluoride level reached 0.5 ppm and the lead level reached 10 ppb. The results showed that the suction filtration capacity of HC for lead ions is 1800 mL/g, and the suction filtration capacity of HCL 2 for fluoride is 1350 mL/g.

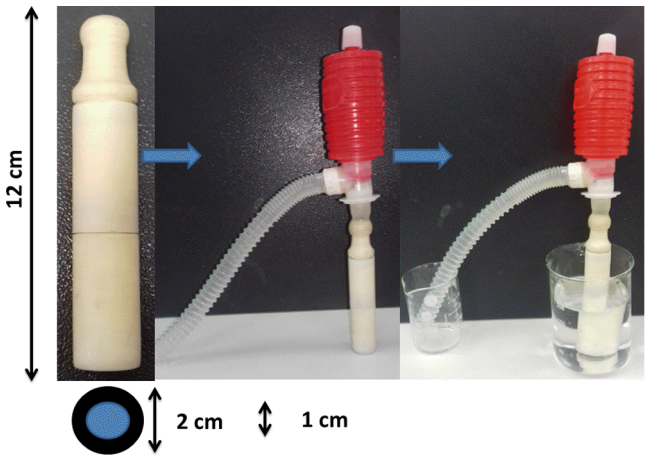


**Figure 10.** Straw filter setup.

Table 6 shows a summary of adsorption capacities, pH, and equilibrium time for some reported materials, and compared to the available literature data, our developed lanthanide-incorporated HAP showed superior ability to scavenge fluoride and exhibited the highest ever recorded adsorption values. On the other hand, versatile adsorbents that can remove both fluorides and lead ions are rarely reported. There are some reports on the removal of both lead ions and fluorides; however, adsorption capacities are not significant. Comparatively, our adsorbents show a considerably high adsorption capacity toward fluoride and lead ions at pH 5.8, proving the versatile nature of adsorbents. Furthermore, the majority of adsorbents reported in the literature require long contact times for equilibrium. However, the equilibrium times of lanthanide-incorporated HAP for fluoride and lead ions adsorption are less than 10 min and less than 30 min, respectively. In addition, most of the early studies were carried out with column-based gravity filtrations, and in here, we have introduced a straw filter prototype under suction filtration.



https://doi.org/10.1021/acsomega.0c05935
ACS Omega 2021, 6, 13527−13543

Table 6. Summary of Adsorption Capacities, pH, and Equilibrium Time for Some Reported Materials

| adsorbent | pH | | equilibrium time (min) | | adsorption capacity (mg/g) | | ref |
|---|---|---|---|---|---|---|---|
| | $F^-$ | $Pb^{2+}$ | $F^-$ | $Pb^{2+}$ | $F^-$ | $Pb^{2+}$ | |
| La- and Ce-modified mesoporous alumina | 5.5−6.5 | | 300 | | 26.4 | | 40 |
| $CeO_2$−$ZrO_2$ nanocages | 3.5−4.5 | | 1440 | | 175 | | 46 |
| $CeO_2$/Mg−Fe layered double hydroxides | 6−7 | | 1440 | | 60.4 | | 35 |
| La−Al-scoria | 7.2 | | 300 | | 23.9 | | 81 |
| La-modified seaweed | 7 | | 240 | | 94.3 | | 82 |
| porous hydroxyapatite | 6.5 | | 1.3 | | 9 | | 83 |
| HAP-MMT | 5 | | 30 | | 16.7 | | 84 |
| Al-HAP | 7 | | 180 | | 98.8 | | 85 |
| CTS-HAP | | 5.5 | | 0.5 | | 909 | 20 |
| nano-hydroxyapatite | | ∼5 | | 600 | | 1300 | 86 |
| CMC-HAP | | 5.5 | | 3 | | 625 | 20 |
| HAP-alginate gelatine | | | | 240 | | 616 | 87 |
| HAP/CTS fibrous composites | | 6 | | 120 | | 162 | 88 |
| hydrous zirconium oxide-impregnated chitosan beads | 3 | 7 | 150 | 150 | 22.1 | 222.2 | 24 |
| coffee-ground-based biosorbent | 4 | 6 | 105 | 75 | 9.05 | 61.6 | 89 |
| HAP·$CeO_2$ (HC) | 5.8 | 5.8 | 4 | 0.5 | 185.2 | 416.0 | this work |
| HAP·$CeO_2$·$La(OH)_3$ 2:1 | 5.8 | 5.8 | 5 | 25 | 200.0 | 212.8 | this work |
| HAP·$CeO_2$·$La(OH)_3$ 3:2 | 5.8 | 5.8 | 4 | 10 | 625.0 | 296.0 | this work |

## 3. EXPERIMENTAL SECTION

**3.1. Materials.** All of the chemicals used in this study were of analytical grade and used without further purification. Lanthanum(III) nitrate hexahydrate (99.999%) and cerium(IV) sulfate were purchased from Sigma-Aldrich Ltd. Calcium nitrate tetrahydrate (98%) from Techno Pharmchem, India, was used in the synthesis along with ammonium monohydrogen phosphate (99%, Sigma-Aldrich). Sodium fluoride (99.5% Merck) was used to prepare the fluoride stock solution.

**3.2. Synthesis of the Hydroxyapatite Ceria Composite (HC).** First, $(NH_4)_2HPO_4$ (12 mmol) and a 30 mL portion of $NH_4OH$ (5 M, 30 mL) were added dropwise to the heated solution of $Ca(NO_3)_2{\cdot}4H_2O$ (20 mmol) wherein the temperature of the solution is 60 °C and the pH of the solution is 10. $Ce(SO_4)_2{\cdot}4H_2O$ (30 mmol) and NaOH (120 mmol) were added to the mixture. The reaction mixture was purged with air and reacted at 80 °C for 3 h while refluxing. The formed yellow precipitate was filtered and washed with water and ethanol sequentially and then dried.

**3.3. Synthesis of Lanthanum-Incorporated Hydroxyapatite Ceria (System 1: Ce/La (2:1); and System II: Ce/La (3:2)).** *3.3.1. System 1: Ce/La (2:1)—(HCL 1).* First, $(NH_4)_2HPO_4$ (12 mmol) and a 30 mL portion of $NH_4OH$ (5 M, 30 mL) were added dropwise to the heated solution of $Ca(NO_3)_2{\cdot}4H_2O$ (20 mmol) wherein the temperature of the solution is 60 °C and the pH of the solution is 10. $Ce(SO_4)_2{\cdot}4H_2O$ (30 mmol), $La(NO_3)_2$ (15 mmol), and NaOH (165 mmol) were added to the mixture. The reaction mixture was purged with air and reacted at 80 °C for 3 h while refluxing. The formed yellow precipitate was filtered and washed with water and ethanol sequentially and dried.

*3.3.2. System II: Ce/La (3:2)—(HCL 2).* The composite was synthesized from the procedure documented in system I and using 20 mmol of $La(NO_3)_2$ and 180 mmol of NaOH.

**3.4. Characterizations.** The morphological studies of the synthesized composites were carried out using scanning electron microscopy (Zeiss Gemini SEM 300). The elemental composition of the composite was analyzed using a SEM-EDX analyzer (Zeiss Gemini SEM 300). The crystal structures of the composites were examined using an X-ray diffractometer (XRD) (Rigaku, Smartlab with Cu K$\alpha$, 0.02° step size and 15°/min scanning speed). The surface elemental analysis of the composite before and after fluoride and lead ion adsorption was performed using X-ray photoelectron spectroscopy (XPS). The XPS system (Thermo Fisher Scientific, U.K.) with an X-ray source of Al K$\alpha$ (1486.6 eV) was equipped to an ultrahigh-vacuum chamber (base pressure better than $2 \times 10^{-8}$ Pa) for the XPS measurements. XPS spectra of the survey with a high pass energy (PE) and the core level with a low PE were performed in the constant analyzer energy (CAE) mode with a pass energy of 50−200 eV and an energy step of 0.1 eV. The presence of functional groups was confirmed using an FT-IR spectrometer (Varian 660-IR). Surface area and average pore size were measured using the Brunauer−Emmett−Teller (BET) analysis with an automated gas sorption analyzer (Autosorb iQ-MP (1 stat), Viton). The colloidal stability of the composite was measured using a Zetasizer (Malvern, ver.7.2). The lead ion concentration of samples was measured by a microwave plasma atomic emission spectrometer (MP-AES) (Agilent, 4210). The fluoride ion concentration was determined using an Orion fluoride ion selective electrode.

**3.5. Adsorption Batch Experiment.** Batch adsorption experiments for lead and fluoride ions were carried out using 0.02 g of HAP·$CeO_2$ (HC), HAP·$CeO_2$·$La(OH)_3$ (2:1) (HCL 1), and HAP·$CeO_2$·$La(OH)_3$ (3:2) (HCL 2) in 50 mL polypropylene vials containing 10 mL of fluoride solution at concentrations ranging from 0.07 to 2.8 g/L and the solution pH was 5.8. Also, the lead ion adsorption isotherm studies were carried out using a 0.07−1 g/L lead ion solution and using 0.02 g of HC, HCL 1, and HCL 2 composites. The mixture was stirred at 180 rpm until it reached equilibrium, and residual fluoride levels and lead ion levels were determined using the Orion fluoride ion selective electrode and MP-AES, respectively.

The lead and fluoride ion adsorption capacities ($q_e$) were calculated using eq 1 as follows[90]

$$q_e = \frac{V}{m}(C_o - C_e) \tag{11}$$



https://doi.org/10.1021/acsomega.0c05935
ACS Omega 2021, 6, 13527−13543

Two linear isotherm equations (Langmuir and Freundlich), which are widely applied in solid/liquid systems, were used to study the adsorption behavior of composites at equilibrium.

The simplified form of the Langmuir isotherm model can be expressed as follows

$$\frac{C_e}{q_e} = \frac{C_e}{q_m} + \frac{1}{Kq_m} \tag{12}$$

where $C_e$ (mg/L) is the equilibrium concentration, $q_e$ is the adsorption capacity at equilibrium, $q_m$ represents the maximum adsorption capacity, and $K$ is the Langmuir constant. The model describes the monolayer retaining of adsorbate on the adsorbent surface with energetically equivalent and identical binding sites.[19,91,92]

The Freundlich adsorption isotherms express the adsorption phenomena on a heterogeneous surface, which have exponential distribution of active sites.[93,94] The linearized form of the equation can be written as follows

$$\ln q_e = \ln K_f + \frac{1}{n} \ln C_e \tag{13}$$

where $C_e$ (mg/L) is the equilibrium concentration, $q_e$ is the adsorbed amount of adsorbate at equilibrium, $K_f$ (L/mg) is the temperature-dependent Freundlich isothermal constant, and "$n$" is a parameter indicating the intensity of adsorption, which differs with the heterogeneous nature of the adsorbent. Values of $n$ between 1 and 10 indicate the multilayer adsorption of the adsorbate.

**3.6. Adsorption Kinetic Studies.** To identify the structure−activity relationship of lanthanide-incorporated HAP further, the involvement of these composites on the sorption rate of lead and fluoride ions was determined. In this circumstance, the adsorption kinetic of fluoride was continuously monitored using a fluoride ion selective electrode from a 0.5 to 60 min time period at three different temperatures using 0.2 g of adsorbent and 30 mL of 10 ppm fluoride solution and the system was continuously stirred (180 rpm). Adsorption kinetics of lead ions was also studied using MP-AES. In this case, 0.025 g of adsorbent in 10 mL of 600 ppm lead ion solution was stirred in a series of different contact times (from 0.5 to 60 min). The spent HC, HCL 1, and HCL 2 were collected for further characterization using SEM-EDX, XPS, and XRD.

The collected kinetic data were interpreted using two kinetic models, namely, the Lagergren-first-order model and Ho's pseudo-second-order model, and thereby the mechanism of adsorption was further investigated.[19]

The linearized form of the Lagergren-first-order rate model can be expressed as follows

$$\ln(q_e - q_t) = \ln q_e - k_1 t \tag{14}$$

where $q_e$ and $q_t$ are the adsorption capacities (mg/g) at equilibrium and at time $t$, respectively, and $k_1$ is the rate constant of the adsorption process.[1,19,83]

The linearized form of Ho's pseudo-second-order rate model can be expressed as

$$\frac{1}{q_t} = \frac{1}{k_2 q_e^2}\left(\frac{1}{t}\right) + \frac{1}{q_e} \tag{15}$$

where $q_e$ and $q_t$ are the adsorption capacities (mg/g) at equilibrium and at time $t$, respectively, and $k_2$ is the rate constant of the pseudo-second-order adsorption process.[1,19]

**3.7. Adsorption Thermodynamics.** The effect of temperature on lead and fluoride adsorption was studied at three different temperatures. In this case, the Arrhenius equation (eq 16) was used to study the apparent activation energy of the adsorption process and the dependence of the apparent rate constant on temperature.[1,19]

$$\ln k_{ap} = \ln A - \frac{E_a}{RT} \tag{16}$$

where $k_{ap}$ is the apparent rate constant, $A$ is the frequency factor, $E_a$ is the activation energy, $T$ is the temperature (K), and $R$ is the universal gas constant.

$$\Delta G^\circ = -RT \ln K_d \tag{17}$$

The thermodynamic parameters such as heat of enthalpy ($\Delta H$), entropy change ($\Delta S$), and Gibbs free energy ($\Delta G$) are very useful parameters to detect the spontaneity and the feasibility of fluoride and lead ion adsorption onto the lanthanide-incorporated HAP. These thermodynamic parameters were calculated using eqs 17−20.[1,19]

where $K_d$ is the thermodynamic distribution coefficient, $T$ is the temperature (K), and $R$ is the universal gas constant.

$$K_d = \frac{q_e}{C_e} \tag{18}$$

where $q_e$ is the amount of adsorbate adsorbed on lanthanide-incorporated HAP at equilibrium (mg/g) and $C_e$ is the equilibrium concentration of the adsorbate in solution.[19] According to the thermodynamic law, the relationship of $\Delta H^\circ$, $\Delta S^\circ$, and $\Delta G^\circ$ of adsorption can be expressed as follows[1,19]

$$\Delta G^\circ = \Delta H^\circ - T\Delta S^\circ \tag{19}$$

The substitution of eqs 17 and 19 results in the below equation[95]

$$\ln K_d = -\frac{\Delta H^\circ}{RT} + \frac{\Delta S^\circ}{R} \tag{20}$$

where $T$ is the temperature (K) and $R$ is the universal gas constant.

**3.8. Influence of pH on the Fluoride and Lead Ion Uptake Capacity.** The influence of pH on the lead and fluoride ion uptake capacity was studied by adjusting the pH of the system from 1 to 6 for lead ions and from 1 to 8 for fluoride using 0.1 M HCl and NaOH (0.02 g/10 mL at 180 rpm and 27 °C). The pH of the system and residual lead and fluoride ion levels were determined using a pH electrode, a fluoride ion selective electrode, and MP-AES, respectively.

**3.9. Effect of Coexisting Ions on $Pb^{2+}$ and $F^-$ Removal.** The effect of coexisting cations on $Pb^{2+}$ removal was studied in the presence of other cations such as $Cd^{2+}$ (100 ppm), $Ca^{2+}$ (100 ppm), and $Mg^{2+}$ (100 ppm) and 0.02 g of adsorbent. Also, the effects of other anions such as $SO_4^{2-}$ (100 ppm), $Cl^-$ (100 ppm), $HCO_3^-$ (100 ppm), and $NO_3^-$ (100 ppm) on $F^-$ removal were studied using 0.02 g of adsorbent and 10 mL of each solution.

**3.10. Leaching Study.** The variation of stability during lead and fluoride ion adsorption was studied using 100 and 1 ppm lead ion as well as fluoride solutions and 0.02 g of HC, HCL 1, and HCL 2 composites. The system was continuously monitored for possible leachates such as calcium, cerium, and lanthanum ions from the 0.5 to 60 min time period.

**3.11. Point of Zero Charge and $\zeta$ Potential of the Composite at pH 5.8.** In this case, a previously reported



https://doi.org/10.1021/acsomega.0c05935
ACS Omega 2021, 6, 13527−13543

procedure[1] was followed with five samples of different pH values (from 2 to 10 and 0.05 g of adsorbent). After 24 h, change in pH of the five different systems was measured and the pH change was plotted as a function of the initial pH to detect the $pH_{pzc}$. Also, the $\zeta$ potential of the colloidal dispersion of three different composites at pH 5.8 was measured using a Malvern zetasizer to detect the stability of dispersions.

## 4. CONCLUSIONS

In this study, an in situ wet chemical precipitation method was used to decorate and fabricate the HAP with lanthanum and cerium ions to synthesize the lanthanide-incorporated nanohydroxyapatite. To enhance the removal of fluoride and lead ions from contaminated water, the ratio of cerium and lanthanum ions was tuned and formed three composites: HAP-$CeO_2$ (HC), HAP·$CeO_2$·$La(OH)_3$ (2:1) (HCL 1), and HAP·$CeO_2$·$La(OH)_3$ (3:2) (HCL 2) composites. The saturation lead ion adsorption capacities of HC, HCL 1, and HCL 2 are 416 mg/g (Langmuir), 213 mg/g (Langmuir), and 296 mg/g (Freundlich), respectively. The saturation fluoride adsorption capacities of HC, HCL 1, and HCL 2 are 185.2 mg/g (Freundlich), 200 mg/g (Langmuir), and 625 mg/g (Langmuir), respectively. The pseudo-second-order kinetic model was provided the best correlation for both $Pb^{2+}$ and $F^-$ adsorption. The postadsorption XRD analysis, XPS analysis, and kinetic and leaching analyses proved the chemisorption behavior during fluoride and lead ion adsorption onto these composites. The thermodynamic profile of the composites follows the same pattern for both lead and fluoride ions, i.e., $\Delta G^\circ < 2$, $\Delta H^\circ > 0$, and $\Delta S^\circ > 0$. As an overview, the HAP·$CeO_2$·$La(OH)_3$ (3:2) (HCL 2) composite material is a better solution for adsorbate-specific customized water filters such as the fluoride water filter due to the high adsorption capacity and the zero leaching effect during fluoride adsorption. For general-purpose water filters that are designed to remove both cations and anions, the HAP-$CeO_2$ (HC) composite material is the most promising approach.

## ■ ASSOCIATED CONTENT

### Supporting Information

The Supporting Information is available free of charge at https://pubs.acs.org/doi/10.1021/acsomega.0c05935.

Surface characterization data such as SEM, EDX, and BET graphs (Figures S1−S7), graphs of temperature study (Figures S8−S10), graphs for the coexisting ion analysis (Figures S11 and S12), graphs for leaching studies (Figure S13), graphs for point of zero charge analysis and $\zeta$ potential analysis (Figures S14 and S15), table for XPS and EDX data comparison and tables for the $X^2$ and linear regression coefficient ($R^2$) value comparison (PDF)

## ■ AUTHOR INFORMATION


### Corresponding Author

**Rohini M. de Silva** − *Centre for Advanced Materials and Devices (CAMD), Department of Chemistry, University of Colombo, Colombo 00300, Sri Lanka;* orcid.org/0000-0003-0955-6366; Email: rohini@chem.cmb.ac.lk

### Authors

**A. K. D. Veromee Kalpana Wimalasiri** − *Centre for Advanced Materials and Devices (CAMD), Department of Chemistry, University of Colombo, Colombo 00300, Sri Lanka*

**M. Shanika Fernando** − *Centre for Advanced Materials and Devices (CAMD), Department of Chemistry, University of Colombo, Colombo 00300, Sri Lanka*

**Karolina Dziemidowicz** − *UCL School of Pharmacy, University College London, London WC1N 1AX, U.K.*

**Gareth R. Williams** − *UCL School of Pharmacy, University College London, London WC1N 1AX, U.K.;* orcid.org/0000-0002-3066-2860

**K. Rasika Koswattage** − *Faculty of Technology, University of Sabaragamuwa, 70140 Belihuloya, Sri Lanka*

**D. P. Dissanayake** − *Centre for Advanced Materials and Devices (CAMD), Department of Chemistry, University of Colombo, Colombo 00300, Sri Lanka;* orcid.org/0000-0002-6213-5782

**K. M. Nalin de Silva** − *Centre for Advanced Materials and Devices (CAMD), Department of Chemistry, University of Colombo, Colombo 00300, Sri Lanka;* orcid.org/0000-0003-3219-3233

Complete contact information is available at: https://pubs.acs.org/10.1021/acsomega.0c05935


### Author Contributions

The manuscript was written through contributions of all authors.

### Notes

The authors declare no competing financial interest.

## ■ ACKNOWLEDGMENTS

The authors gratefully acknowledge the National Research Council Sri Lanka (NRC TO 16-18) for the financial support provided and University of Moratuwa and UCL School of Pharmacy, University College London, for providing the scanning electron microscope (SEM) and X-ray photoelectron spectroscopy (XPS) facilities.

## ■ REFERENCES


(1) Raghav, S.; Kumar, D. Adsorption Equilibrium, Kinetics, and Thermodynamic Studies of Fluoride Adsorbed by Tetrametallic Oxide Adsorbent. *J. Chem. Eng. Data* **2018**, *63*, 1682−1697.

(2) Qiao, X.; Liu, G.; Wang, J.; Zhang, Y. Highly Efficient and Selective Removal of Lead Ions from Aqueous Solutions by Conjugated Microporous Polymers with Functionalized Heterogeneous Pores. *Cryst. growth Des.* **2020**, 337.

(3) Yu, C.-C.; Lin, J.-L.; Lin-Tan, D.-T. Environmental Exposure to Lead and Progression of Chronic Renal Diseases: A Four-Year Prospective Longitudinal Study. *J. Am. Soc. Nephrol.* **2004**, *15*, 1016−1022.

(4) Cleveland, L. M.; Minter, M. L.; Cobb, K. A.; Scott, A. A.; German, V. F. Lead Hazards for Pregnant Women and Children: Part 1 and Children: Part 1: Immigrants and the Poor Shoulder Most of the Burden of Lead Exposure in This Country. Part 1 of a Two-Part Article Details How Exposure Happens, Whom It Affects, and the Harm It Can Do. *Am. J. Nurs.* **2008**, *108*, 40−49.

(5) Sokol, R. Z.; Berman, N. The Effect of Age of Exposure on Lead-Induced Testicular Toxicity. *Toxicology* **1991**, *69*, 269−278.

(6) Wani, A. L.; Ara, A.; Usmani, J. A. Lead Toxicity: A Review. *Interdiscip. Toxicol.* **2015**, 55−64.

(7) Wickramarathna, S.; Balasooriya, S.; Diyabalanage, S.; Chandrajith, R. Tracing Environmental Aetiological Factors of Chronic Kidney Diseases in the Dry Zone of Sri Lanka—A Hydrogeochemical and Isotope Approach. *J. Trace Elem. Med. Biol.* **2017**, *44*, 298−306.

(8) Dey, S.; Goswami, S.; Ghosh, U. C. Hydrous Ferric Oxide (HFO) - A Scavenger for Fluoride from Contaminated Water. *Water, Air, Soil Pollut.* **2004**, 311.

(9) Dhar, V.; Bhatnagar, M. Physiology and Toxicity of Fluoride. *Indian J. Dent. Res.* **2009**, *20*, 350.
(10) Fan, X.; Parker, D. J.; Smith, M. D. Adsorption Kinetics of Fluoride on Low Cost Materials. *Water Res.* **2003**, *37*, 4929−4937.
(11) Das, N.; Pattanaik, P.; Das, R. Defluoridation of Drinking Water Using Activated Titanium Rich Bauxite. *J. Colloid Interface Sci.* **2005**, *292*, 1−10.
(12) Huang, H.; Liu, J.; Zhang, P.; Zhang, D.; Gao, F. Investigation on the Simultaneous Removal of Fluoride, Ammonia Nitrogen and Phosphate from Semiconductor Wastewater Using Chemical Precipitation. *Chem. Eng. J.* **2017**, *307*, 696−706.
(13) Ndiaye, P. I.; Moulin, P.; Dominguez, L.; Millet, J. C.; Charbit, F. Removal of Fluoride from Electronic Industrial Effluentby RO Membrane Separation. *Desalination* **2005**, *173*, 25−32.
(14) Le, N. L.; Nunes, S. P. Materials and Membrane Technologies for Water and Energy Sustainability. *Sustainable Mater. Technol.* **2016**, *7*, 1−28.
(15) Arora, M.; Maheshwari, R. C.; Jain, S. K.; Gupta, A. Use of Membrane Technology for Potable Water Production. *Desalination* **2004**, *170*, 105−112.
(16) Hu, K.; Dickson, J. M. Nanofiltration Membrane Performance on Fluoride Removal from Water. *J. Membr. Sci.* **2006**, *279*, 529−538.
(17) Boubakri, A.; Helali, N.; Tlili, M.; Amor, M. Ben. Fluoride Removal from Diluted Solutions by Donnan Dialysis Using Full Factorial Design. *Korean J. Chem. Eng.* **2014**, *31*, 461−466.
(18) Kabay, N.; Arar, Ö.; Samatya, S.; Yüksel, Ü.; Yüksel, M. Separation of Fluoride from Aqueous Solution by Electrodialysis: Effect of Process Parameters and Other Ionic Species. *J. Hazard. Mater.* **2008**, *153*, 107−113.
(19) Ge, Y.; Qin, L.; Li, Z. Lignin Microspheres: An Effective and Recyclable Natural Polymer-Based Adsorbent for Lead Ion Removal. *Mater. Des.* **2016**, *95*, 141−147.
(20) Manatunga, D. C.; De Silva, R. M.; De Silva, K. M. N.; Ratnaweera, R. Natural Polysaccharides Leading to Super Adsorbent Hydroxyapatite Nanoparticles for the Removal of Heavy Metals and Dyes from Aqueous Solutions. *RSC Adv.* **2016**, *6*, 105618−105630.
(21) Wijesinghe, W. P. S. L.; Mantilaka, M. M. M. G. P. G.; Peiris, T. A. N.; Rajapakse, R. M. G.; Wijayantha, K. G. U.; Pitawala, H. M. T. G. A.; Premachandra, T. N.; Herath, H. M. T. U.; Rajapakse, R. P. V. J. Preparation and Characterization of Mesoporous Hydroxyapatite with Non-Cytotoxicity and Heavy Metal Adsorption Capacity. *New J. Chem.* **2018**, *42*, 10271−10278.
(22) Fernando, M. S.; De Silva, R. M.; De Silva, K. M. N. Synthesis, Characterization, and Application of Nano Hydroxyapatite and Nanocomposite of Hydroxyapatite with Granular Activated Carbon for the Removal of Pb2+ from Aqueous Solutions. *Appl. Surf. Sci.* **2015**, *351*, 95−103.
(23) Babel, S.; Kurniawan, T. A. Low-Cost Adsorbents for Heavy Metals Uptake from Contaminated Water: A Review. *J. Hazard. Mater.* **2003**, *97*, 219−243.
(24) Srivastava, S. K.; Bhattacharjee, G.; Tyagi, R.; Pant, N.; Pal, N. Studies on the Removal of Some Toxic Metal Ions from Aqueous Solutions and Industrial Waste. Part I (Removal of Lead and Cadmium by Hydrous Iron and Aluminium Oxide). *Environ. Technol. Lett.* **1988**, *9*, 1173−1185.
(25) Maliyekkal, S. M.; Sharma, A. K.; Philip, L. Manganese-Oxide-Coated Alumina: A Promising Sorbent for Defluoridation of Water. *Water Res.* **2006**, *40*, 3497−3506.
(26) Teutli-Sequeira, A.; Martínez-Miranda, V.; Solache-Ríos, M.; Linares-Hernández, I. Aluminum and Lanthanum Effects in Natural Materials on the Adsorption of Fluoride Ions. *J. Fluorine Chem.* **2013**, *148*, 6−13.
(27) Viswanathan, N.; Meenakshi, S. Enriched Fluoride Sorption Using Alumina/Chitosan Composite. *J. Hazard. Mater.* **2010**, *178*, 226−232.
(28) Nie, Y.; Hu, C.; Kong, C. Enhanced Fluoride Adsorption Using Al (III) Modified Calcium Hydroxyapatite. *J. Hazard. Mater.* **2012**, *233*−*234*, 194−199.
(29) Sakhare, N.; Lunge, S.; Rayalu, S.; Bakardjiva, S.; Subrt, J.; Devotta, S.; Labhsetwar, N. Defluoridation of Water Using Calcium Aluminate Material. *Chem. Eng. J.* **2012**, *203*, 406−414.
(30) Sujana, M. G.; Anand, S. Iron and Aluminium Based Mixed Hydroxides: A Novel Sorbent for Fluoride Removal from Aqueous Solutions. *Appl. Surf. Sci.* **2010**, *256*, 6956−6962.
(31) Ndé-Tchoupé, A. I.; Crane, R. A.; Mwakabona, H. T.; Noubactep, C.; Njau, K. N. Technologies for Decentralized Fluoride Removal: Testing Metallic Iron-Based Filters. *Water* **2015**, *7*, 6750−6774.
(32) Dou, X.; Zhang, Y.; Wang, H.; Wang, T.; Wang, Y. Performance of Granular Zirconium−Iron Oxide in the Removal of Fluoride from Drinking Water. *Water Res.* **2011**, *45*, 3571−3578.
(33) Chai, L.; Wang, Y.; Zhao, N.; Yang, W.; You, X. Sulfate-Doped Fe3O4/Al2O3 Nanoparticles as a Novel Adsorbent for Fluoride Removal from Drinking Water. *Water Res.* **2013**, *47*, 4040−4049.
(34) Velazquez-Jimenez, L. H.; Hurt, R. H.; Matos, J.; Rangel-Mendez, J. R. Zirconium−Carbon Hybrid Sorbent for Removal of Fluoride from Water: Oxalic Acid Mediated Zr(IV) Assembly and Adsorption Mechanism. *Environ. Sci. Technol.* **2014**, *48*, 1166−1174.
(35) Zhang, T.; Li, Q.; Xiao, H.; Mei, Z.; Lu, H.; Zhou, Y. Enhanced Fluoride Removal from Water by Non-Thermal Plasma Modified CeO2/Mg−Fe Layered Double Hydroxides. *Appl. Clay Sci.* **2013**, *72*, 117−123.
(36) Huang, P.-P.; Cao, C.-Y.; Wei, F.; Sun, Y.-B.; Song, W.-G. MgAl Layered Double Hydroxides with Chloride and Carbonate Ions as Interlayer Anions for Removal of Arsenic and Fluoride Ions in Water. *RSC Adv.* **2015**, *5*, 10412−10417.
(37) Yu, X.; Tong, S.; Ge, M.; Zuo, J. Removal of Fluoride from Drinking Water by Cellulose@hydroxyapatite Nanocomposites. *Carbohydr. Polym.* **2013**, *92*, 269−275.
(38) Pandi, K.; Viswanathan, N. Synthesis of Alginate Bioencapsulated Nano-Hydroxyapatite Composite for Selective Fluoride Sorption. *Carbohydr. Polym.* **2014**, *112*, 662−667.
(39) Yu, Y.; Wang, C.; Guo, X.; Paul Chen, J. Modification of Carbon Derived from Sargassum Sp. by Lanthanum for Enhanced Adsorption of Fluoride. *J. Colloid Interface Sci.* **2015**, *441*, 113−120.
(40) He, Y.; Zhang, L.; An, X.; Wan, G.; Zhu, W.; Luo, Y. Enhanced Fluoride Removal from Water by Rare Earth (La and Ce) Modified Alumina: Adsorption Isotherms, Kinetics, Thermodynamics and Mechanism. *Sci. Total Environ.* **2019**, *688*, 184−198.
(41) Zhang, Y.; Lin, X.; Zhou, Q.; Luo, X. Fluoride Adsorption from Aqueous Solution by Magnetic Core-Shell Fe 3 O 4 @alginate-La Particles Fabricated via Electro-Coextrusion. *Appl. Surf. Sci.* **2016**, *389*, 34−45.
(42) Wang, L.; Xie, Y.; Yang, J.; Zhu, X.; Hu, Q.; Li, X.; Liu, Z. Insight into Mechanisms of Fluoride Removal from Contaminated Groundwater Using Lanthanum-Modified Bone Waste. *RSC Adv.* **2017**, *7*, 54291−54305.
(43) Jagtap, S.; Yenkie, M. K.; Das, S.; Rayalu, S. Synthesis and Characterization of Lanthanum Impregnated Chitosan Flakes for Fluoride Removal in Water. *Desalination* **2011**, *273*, 267−275.
(44) Vences-Alvarez, E.; Velazquez-Jimenez, L. H.; Chazaro-Ruiz, L. F.; Diaz-Flores, P. E.; Rangel-Mendez, J. R. Fluoride Removal in Water by a Hybrid Adsorbent Lanthanum-Carbon. *J. Colloid Interface Sci.* **2015**, *455*, 194−202.
(45) Ghosh, A.; Chakrabarti, S.; Biswas, K.; Ghosh, U. C. Agglomerated Nanoparticles of Hydrous Ce(IV) + Zr(IV) Mixed Oxide: Preparation, Characterization and Physicochemical Aspects on Fluoride Adsorption. *Appl. Surf. Sci.* **2014**, *307*, 665−676.
(46) Wang, J.; Xu, W.; Chen, L.; Jia, Y.; Wang, L.; Huang, X.; Liu, J. Excellent Fluoride Removal Performance by CeO 2 − ZrO 2 Nanocages in Water Environment. *Chem. Eng. J.* **2013**, *231*, 198−205.
(47) Sivasankar, V.; Murugesh, S.; Rajkumar, S.; Darchen, A. Cerium Dispersed in Carbon (CeDC) and Its Adsorption Behavior: A First Example of Tailored Adsorbent for Fluoride Removal from Drinking Water. *Chem. Eng. J.* **2013**, *214*, 45−54.


https://doi.org/10.1021/acsomega.0c05935
*ACS Omega* 2021, 6, 13527−13543

(48) Lin, J.; Wu, Y.; Khayambashi, A.; Wang, X.; Wei, Y. Preparation of a Novel $CeO_2$ /$SiO_2$ Adsorbent and Its Adsorption Behavior for Fluoride Ion. *Adsorpt. Sci. Technol.* **2018**, *36*, 743−761.
(49) Liu, H.; Deng, S.; Li, Z.; Yu, G.; Huang, J. Preparation of Al-Ce Hybrid Adsorbent and Its Application for Defluoridation of Drinking Water. *J. Hazard. Mater.* **2010**, *179*, 424−430.
(50) Dahle, J. T.; Arai, Y. Environmental Geochemistry of Cerium: Applications and Toxicology of Cerium Oxide Nanoparticles. *Int. J. Environ. Res. Public Health* **2015**, *12*, 1253−1278.
(51) Chouaib, F.; Delgado, G.; Beaunier, P.; Picard, G. Characterization of Cerium Oxides Prepared in Water and Sodium Hydroxide Mixtures. *J. Alloys Compd.* **1992**, *185*, 279−293.
(52) Chen, H. I.; Chang, H. Y. Synthesis of Nanocrystalline Cerium Oxide Particles by the Precipitation Method. *Ceram. Int.* **2005**, *31*, 795−802.
(53) Yasukawa, A.; Gotoh, K.; Tanaka, H.; Kandori, K. Preparation and Structure of Calcium Hydroxyapatite Substituted with Light Rare Earth Ions. *Colloids Surf., A* **2012**, *393*, 53−59.
(54) Wijesinghe, W. P. S. L.; Mantilaka, M. M. M. G. P. G.; Peiris, T. A. N.; Rajapakse, R. M. G.; Wijayantha, K. G. U.; Pitawala, H. M. T. G. A.; Premachandra, T. N.; Herath, H. M. T. U.; Rajapakse, R. P. V. J. Preparation and Characterization of Mesoporous Hydroxyapatite with Non-Cytotoxicity and Heavy Metal Adsorption Capacity. *New J. Chem.* **2018**, *42*, 10271−10278.
(55) Wu, X.; Song, X.; Li, D.; Liu, J.; Zhang, P.; Chen, X. Preparation of Mesoporous Nano-Hydroxyapatite Using a Surfactant Template Method for Protein Delivery. *J. Bionic Eng.* **2012**, *9*, 224−233.
(56) In, Y.; Amornkitbamrung, U.; Hong, M.-H.; Shin, H. On the Crystallization of Hydroxyapatite under Hydrothermal Conditions: Role of Sebacic Acid as an Additive. *ACS Omega* **2020**, *5*, 27204−27210.
(57) Iconaru, S. L.; Motelica-Heino, M.; Predoi, D. Study on Europium-Doped Hydroxyapatite Nanoparticles by Fourier Transform Infrared Spectroscopy and Their Antimicrobial Properties. *J. Spectrosc.* **2013**, *1*, No. 284285.
(58) Phatai, P.; Futalan, C. M.; Utara, S.; Khemthong, P.; Kamonwannasit, S. Structural Characterization of Cerium-Doped Hydroxyapatite Nanoparticles Synthesized by an Ultrasonic-Assisted Sol-Gel Technique. *Results Phys.* **2018**, *10*, 956−963.
(59) Ciobanu, C. S.; Iconaru, S. L.; Le Coustumer, P.; Predoi, D. Vibrational Investigations of Silver-Doped Hydroxyapatite with Antibacterial Properties. *J. Spectrosc.* **2013**, *1*, No. 471061.
(60) Sawana, R.; Somasundar, Y.; Iyer, V. S.; Baruwati, B. Ceria Modified Activated Carbon: An Efficient Arsenic Removal Adsorbent for Drinking Water Purification. *Appl. Water Sci.* **2017**, *7*, 1223−1230.
(61) Ratnayake, S. P.; Mantilaka, M. M. M. G. P. G.; Sandaruwan, C.; Dahanayake, D.; Gunasekara, Y. P.; Jeyasakthy, S.; Gurusinghe, N. M.; Wanninayake, U. K.; Nalin de Silva, K. M. Low-Temperature Thermocatalytic Particulate Carbon Decomposition via Urea Solution-Combustion Derived $CeO_2$ Nanostructures. *J. Rare Earths* **2021**, *67*.
(62) Aglan, H. A.; Mabrouk, M.; Aly, R. M.; Beherei, H. H.; Ahmed, H. H. Harnessing the Antioxidant Property of Cerium and Yttrium Oxide Nanoparticles to Enhance Mesenchymal Stem Cell Proliferation. *Asian J. Pharm. Clin. Res.* **2018**, *11*, 436.
(63) Mousavi-kamazani, M.; Alizadeh, S.; Ansari, F.; Salavati-niasari, M. A Controllable Hydrothermal Method to Prepare La (OH) 3 Nanorods Using New Precursors. *J. Rare Earths* **2015**, *33*, 425−431.
(64) Manatunga, D. C.; de Silva, R. M.; Nalin de Silva, K. M.; de Silva, N.; Premalal, E. V. A. Metal and Polymer-Mediated Synthesis of Porous Crystalline Hydroxyapatite Nanocomposites for Environmental Remediation. *R. Soc. Open Sci.* **2018**, *5*, No. 171557.
(65) Miculescu, F.; Maidaniuc, A.; Miculescu, M.; Batalu, N. D.; Ciocoiu, R. C.; Voicu, Ş. I.; Stan, G. E.; Thakur, V. K. Synthesis and Characterization of Jellified Composites from Bovine Bone-Derived Hydroxyapatite and Starch as Precursors for Robocasting. *ACS Omega* **2018**, 1338.
(66) Costescu, A.; Ciobanu, C. S.; Iconaru, S. L.; Ghita, R. V.; Chifiriuc, C. M.; Marutescu, L. G.; Predoi, D. Fabrication, Characterization, and Antimicrobial Activity, Evaluation of Low Silver Concentrations in Silver-Doped Hydroxyapatite Nanoparticles. *J. Nanomater.* **2013**, *2013*, No. 194854.
(67) Mavropoulos, E.; Costa, A. M.; Fiocruz, C.; Leopoldo, R.; Saldanha, M. Studies on the Mechanisms of Lead Immobilization by Hydroxyapatite. *Environ. Sci. Technol.* **2002**, *36*, 1625−1629.
(68) Yeh, J. J.; Lindau, I. Atomic Subshell Photoionization Cross Sections and Asymmetry Parameters: $1 \leqslant Z \leqslant 103$. *At. Data Nucl. Data Tables* **1985**, *32*, 1−155.
(69) Seah, M. P.; Dench, W. A. Quantitative Electron Spectroscopy of Surface. *Surf. Interface Anal.* **1979**, *1*, 2.
(70) Koswattage, K. R.; Shimoyama, I.; Baba, Y.; Sekiguchi, T.; Nakagawa, K. Selective Adsorption of Atomic Hydrogen on a H-BN Thin Film. *J. Chem. Phys.* **2011**, *135*, No. 014706.
(71) Koswattage, K. R.; Shimoyama, I.; Baba, Y.; Sekiguchi, T.; Nakagawa, K. Study on Selective Adsorption of Deuterium on Boron Nitride Using Photon-Stimulated Ion-Desorption. *Appl. Surf. Sci.* **2011**, *258*, 1561−1564.
(72) Fernando, M. S.; Wimalasiri, A. K. D. V. K.; Dziemidowicz, K.; Williams, G. R.; Koswattage, K. R.; Dissanayake, D. P.; de Silva, K. M. N.; de Silva, R. M. Biopolymer-Based Nanohydroxyapatite Composites for the Removal of Fluoride, Lead, Cadmium, and Arsenic from Water. *ACS Omega* **2021**, *6*, 8517.
(73) Li-Yun, C.; Chuan-Bo, Z.; Jian-Feng, H. Influence of Temperature, [Ca2+], Ca/P Ratio and Ultrasonic Power on the Crystallinity and Morphology of Hydroxyapatite Nanoparticles Prepared with a Novel Ultrasonic Precipitation Method. *Mater. Lett.* **2005**, *59*, 1902−1906.
(74) Gorzalski, A. S.; Donley, C.; Coronell, O. Elemental Composition of Membrane Foulant Layers Using EDS, XPS, and RBS. *J. Membr. Sci.* **2017**, *522*, 31−44.
(75) Ho, Y. Isotherms for the Sorption of Lead onto Peat: Comparison of Linear and Non-Linear Methods. *Pol. J. Environ. Stud.* **2006**, *15*, 81−86.
(76) Chabani, M.; Amrane, A.; Bensmaili, A. Equilibrium Sorption Isotherms for Nitrate on Resin Amberlite IRA 400. *J. Hazard. Mater.* **2009**, *165*, 27−33.
(77) Plakhova, T. V.; Romanchuk, A. Y.; Yakunin, S. N.; Dumas, T.; Demir, S.; Wang, S.; Minasian, S. G.; Shuh, D. K.; Tyliszczak, T.; Shiryaev, A. A.; et al. Solubility of Nanocrystalline Cerium Dioxide: Experimental Data and Thermodynamic Modeling. *J. Phys. Chem. C* **2016**, *120*, 22615−22626.
(78) Aharchaou, I.; Beaubien, C.; Campbell, P. G. C.; Fortin, C. Lanthanum and Cerium Toxicity to the Freshwater Green Alga *Chlorella fusca*: Applicability of the Biotic Ligand Model. *Environ. Toxicol. Chem.* **2020**, *39*, 996−1005.
(79) Sneller, F. E. C.; Kalf, D. F.; Weltje, L.; Van Wezel, A. P. *Maximum Permissible Concentrations and Negligible Concentrations for Rare Earth Elements (REEs)*; RIVM, 2000.
(80) Iconaru, S. L.; Prodan, A. M.; Buton, N.; Predoi, D.; Vasilev, K.; Cavallaro, A.; Zilm, P. Structural Characterization and Antifungal Studies of Zinc-Doped Hydroxyapatite Coatings. *Molecules* **2017**, No. 604.
(81) Zhang, S.; Lu, Y.; Lin, X.; Su, X.; Zhang, Y. Removal of Fluoride from Groundwater by Adsorption onto La (III) - Al (III) Loaded Scoria Adsorbent. *Appl. Surf. Sci.* **2014**, *303*, 1−5.
(82) Yu, Y.; Wang, C.; Guo, X.; Chen, J. P. Modification of Carbon Derived from Sargassum Sp. by Lanthanum for Enhanced Adsorption of Fluoride. *J. Colloid Interface Sci.* **2015**, 113−120.
(83) Wimalasiri, A. K. D. V. K.; Fernando, M. S.; Williams, G. R.; Dissanayake, D. P.; de Silva, K. M. N.; de Silva, R. M. Microwave Assisted Accelerated Fluoride Adsorption by Porous Nanohydroxyapatite. *Mater. Chem. Phys.* **2021**, *257*, No. 123712.
(84) Fernando, M. S.; Wimalasiri, A. K. D. V. K.; Ratnayake, S. P.; Jayasinghe, J. M. A. R. B.; William, G. R.; Dissanayake, D. P.; De Silva, K. M. N.; De Silva, R. M. Improved Nanocomposite of Montmorillonite and Hydroxyapatite for Defluoridation of Water. *RSC Adv.* **2019**, *9*, 35588.


https://doi.org/10.1021/acsomega.0c05935
*ACS Omega* 2021, 6, 13527−13543

(85) He, J.; Chen, K.; et al. A Biocompatible and Novelly-Defined Al-HAP Adsorption Membrane for Highly Effective Removal of Fluoride from Drinking Water. *J. Colloid Interface Sci.* **2017**, *490*, 97−107.
(86) Zhou, C.; Wang, X.; Song, X.; Wang, Y.; Fang, D.; Ge, S.; Zhang, R. Insights into Dynamic Adsorption of Lead by Nano-Hydroxyapatite Prepared with Two-Stage Ultrasound. *Chemosphere* **2020**, *253*, No. 126661.
(87) Sangeetha, K.; Vidhya, G.; Vasugi, G.; Girija, E. K. Lead and Cadmium Removal from Single and Binary Metal Ion Solution by Novel Hydroxyapatite/Alginate/Gelatin Nanocomposites Lead and Cadmium Removal from Single and Binary Metal Ion Solution by Novel Hydroxyapatite/Alginate/Gelatin Nanocomposites. *J. Environ. Chem. Eng.* **2018**, 1118.
(88) Park, S.; Gomez-flores, A.; Chung, Y. S.; Kim, H. Removal of Cadmium and Lead from Aqueous Solution by Hydroxyapatite/Chitosan Hybrid Fibrous Sorbent: Kinetics and Equilibrium Studies. *J. Chem.* **2015**, *2015*, No. 396290.
(89) Naga Babu, A.; Reddy, D. S.; Kumar, G. S.; Ravindhranath, K.; Krishna Mohan, G. V. Removal of Lead and Fluoride from Contaminated Water Using Exhausted Coffee Grounds Based Bio-Sorbent. *J. Environ. Manage.* **2018**, *218*, 602−612.
(90) Adeogun, A. I.; Ofudje, E. A.; Idowu, M. A.; Kareem, S. O.; Vahidhabanu, S.; Ramesh Babu, B. Biowaste-Derived Hydroxyapatite for Effective Removal of Reactive Yellow 4 Dye: Equilibrium, Kinetic, and Thermodynamic Studies. *ACS Omega* **2018**, *3*, 1991−2000.
(91) Nowicki, P.; Kazmierczak-Razna, J.; Pietrzak, R. Physicochemical and Adsorption Properties of Carbonaceous Sorbents Prepared by Activation of Tropical Fruit Skins with Potassium Carbonate. *Mater. Des.* **2016**, *90*, 579−585.
(92) Iconaru, S. L.; Motelica-Heino, M.; Guegan, R.; Predoi, M. V.; Prodan, A. M.; Predoi, D. Removal of Zinc Ions Using Hydroxyapatite and Study of Ultrasound Behavior of Aqueous Media. *Materials* **2018**, *11*, No. 1350.
(93) Kumara, N. T. R. N.; Hamdan, N.; Petra, M. I.; Tennakoon, K. U.; Ekanayake, P. Equilibrium Isotherm Studies of Adsorption of Pigments Extracted from Kuduk-Kuduk (*Melastoma malabathricum* L.) Pulp onto TiO2 Nanoparticles. *J. Chem.* **2014**, *2014*, No. 468975.
(94) Predoi, D.; Iconaru, S. L.; Predoi, M. V.; Motelica-Heino, M. Removal and Oxidation of as(III) from Water Using Iron Oxide Coated CTAB as Adsorbent. *Polymers* **2020**, *12*, No. 1687.
(95) Nayak, B.; Samant, A.; Patel, R.; Misra, P. K. Comprehensive Understanding of the Kinetics and Mechanism of Fluoride Removal over a Potent Nanocrystalline Hydroxyapatite Surface. *ACS Omega* **2017**, *2*, 8118−8128.


https://doi.org/10.1021/acsomega.0c05935
*ACS Omega* 2021, 6, 13527−13543